Biophysical Journal
Biophysical Letter

Biophysical Society

A potential interaction between the SARS-CoV-2 spike protein and nicotinic acetylcholine receptors

A. Sofia F. Oliveira,[1,4] Amaurys Avila Ibarra,[2] Isabel Bermudez,[5] Lorenzo Casalino,[6] Zied Gaieb,[6] Deborah K. Shoemark,[3,4] Timothy Gallagher,[1] Richard B. Sessions,[3] Rommie E. Amaro,[6] and Adrian J. Mulholland[1,*]

[1]Centre for Computational Chemistry, School of Chemistry, [2]Research Software Engineering, Advanced Computing Research Centre, and [3]School of Biochemistry, University of Bristol, Bristol, United Kingdom; [4]Bristol Synthetic Biology Centre, BrisSynBio, Bristol, United Kingdom; [5]Department of Biological and Medical Sciences, Oxford Brookes University, Oxford, United Kingdom; and [6]Department of Chemistry and Biochemistry, University of California San Diego, La Jolla, California

ABSTRACT Changeux et al. (Changeux et al. *C. R. Biol.* 343:33–39.) recently suggested that the SARS-CoV-2 spike protein may interact with nicotinic acetylcholine receptors (nAChRs) and that such interactions may be involved in pathology and infectivity. This hypothesis is based on the fact that the SARS-CoV-2 spike protein contains a sequence motif similar to known nAChR antagonists. Here, we use molecular simulations of validated atomically detailed structures of nAChRs and of the spike to investigate the possible binding of the Y674-R685 region of the spike to nAChRs. We examine the binding of the Y674-R685 loop to three nAChRs, namely the human $\alpha4\beta2$ and $\alpha7$ subtypes and the muscle-like $\alpha\beta\gamma\delta$ receptor from *Tetronarce californica*. Our results predict that Y674-R685 has affinity for nAChRs. The region of the spike responsible for binding contains a PRRA motif, a four-residue insertion not found in other SARS-like coronaviruses. The conformational behavior of the bound Y674-R685 is highly dependent on the receptor subtype; it adopts extended conformations in the $\alpha4\beta2$ and $\alpha7$ complexes but is more compact when bound to the muscle-like receptor. In the $\alpha4\beta2$ and $\alpha\beta\gamma\delta$ complexes, the interaction of Y674-R685 with the receptors forces the loop C region to adopt an open conformation, similar to other known nAChR antagonists. In contrast, in the $\alpha7$ complex, Y674-R685 penetrates deeply into the binding pocket in which it forms interactions with the residues lining the aromatic box, namely with TrpB, TyrC1, and TyrC2. Estimates of binding energy suggest that Y674-R685 forms stable complexes with all three nAChR subtypes. Analyses of simulations of the glycosylated spike show that the Y674-R685 region is accessible for binding. We suggest a potential binding orientation of the spike protein with nAChRs, in which they are in a nonparallel arrangement to one another.

SIGNIFICANCE It was recently suggested that the SARS-CoV-2 spike protein may interact with nicotinic acetylcholine receptors and that such interactions may be involved in pathology and infectivity. We investigate this hypothesis by molecular dynamics simulations. Our results predict that a viral spike protein peptide (adjacent to the furin cleavage site) exhibits favorable binding affinity to nicotinic acetylcholine receptors and suggest subtype-specific dynamics for the peptide. We show that this peptide is accessible in the fully glycosylated spike. We model how the spike may interact with these receptors and find that interaction is possible with the two proteins in a nonparallel arrangement.

INTRODUCTION

The severe acute respiratory syndrome coronavirus-2 (SARS-CoV-2) is a novel strain of coronavirus that first appeared in China in late 2019 and causes the potentially fatal disease coronavirus disease 2019 (COVID-19). This virus initially infects respiratory epithelial cells by binding to the angiotensin-converting 2 enzyme (ACE2) receptor (1). Although predominantly recognized as a respiratory disease (2,3), SARS-CoV-2 also causes severe inflammation and damage in other organs (4–7). Under certain conditions (and as with other coronaviruses (8)), SARS-CoV-2 may enter the central nervous system (CNS) through the bloodstream by disrupting the blood-brain barrier or infecting the peripheral nerves (e.g., (7,9–12)).

Since it emerged as a human pathogen, SARS-CoV-2 has caused more than 80.8 million confirmed cases of COVID-19 and more than 1.7 million deaths worldwide, as of December 28, 2020 (13). Several major risk factors for the development

Submitted November 11, 2020, and accepted for publication January 13, 2021.

*Correspondence: adrian.mulholland@bristol.ac.uk

Editor: Tamar Schlick.

https://doi.org/10.1016/j.bpj.2021.01.037

of COVID-19 have been identified, including age, heart disease, diabetes, and hypertension (14). Given the apparently low prevalence of smokers among hospitalized COVID-19 patients (15–17), it was proposed that nicotine may offer some protective value to mitigate COVID-19 (the "protection" hypothesis) (15). It has been suggested that medicinal nicotine (either in patches, gum, or electronic delivery systems) should be investigated as a therapeutic option for this disease (e.g., (15,18)). Clinical trials for nicotine are underway (e.g., https://clinicaltrials.gov/ct2/show/NCT04429815). Alternative explanations to the protection hypothesis have been proposed (19); the first relates to the failure in correctly identifying smokers upon hospital admission (19) and the second is that hospitalized COVID-19 patients may be less likely to smoke as their comorbidities motivate them to quit ("smoking cessation" hypothesis) (19).

Based on the early observations of the lower-than-expected smoking prevalence in hospitalized COVID-19 patients, Changeux and colleagues suggested a role for nicotinic acetylcholine receptors (nAChRs) in the pathophysiology of COVID-19 via a direct interaction between these receptors and the viral spike glycoprotein (20). This suggestion was based on the fact that the spike protein contains a sequence motif similar to known nAChR antagonists (20) (Fig. S1), such as α-bungarotoxin from *Bungarus multicinctus* and glycoprotein from *Rabies lyssavirus* (formerly *Rabies virus*). Changeux et al. and others also proposed that COVID-19 might be controlled or mitigated by the use of nicotine, if the latter can compete with the virus for binding to these receptors (e.g., (9,18,20–24)). If interactions with nAChRs are important, they may be relevant for some of the systemic effects observed in COVID-19.

nAChRs are cation channels that belong to the pentameric ligand-gated ion channel family (25). They are present in both the peripheral (at the skeletal neuromuscular junction and in the autonomic nervous system) and CNS (26). The neuronal receptors have emerged as important targets for the treatment of Alzheimer's disease, schizophrenia, pain, and nicotine addiction (26,27). Mutations of muscle nAChR can cause congenital myasthenia gravis (27). A large repertoire of nAChR subtypes differ in the homo- or heteromeric assembly of five monomers arranged around a central channel axis (28–30). Each nAChR subtype shows different selectivity for agonists and antagonists (28–30). All nAChRs share the same basic architecture (Fig. 1 *B*), formed of a large N-terminal extracellular domain (ECD), where the agonist-binding site is located; a transmembrane domain (TMD) surrounding the ion channel; an intracellular domain (ICD); and a short extracellular C-terminal domain (CTD) (28–30) The ligand-binding pocket is located at the interface between two neighboring subunits (Fig. 1 *B*) and is formed by loops A, B, and C from the principal subunit and D, E, and F from the complementary subunit (Fig. S2). The $\alpha4\beta2$ nAChR is the most prevalent heteromeric subtype in the brain; it is implicated in diverse processes such as cognition, mood, and reward and is necessary for nicotine addiction (28–30,34). The homomeric $\alpha7$ nAChR is also abundant and widely expressed in the CNS, where it contributes to cognition, sensory processing, and attention (35). The $\alpha7$ subtype is also expressed on a variety of nonneuronal cells, such as immune cells, astrocytes, microglia, and endothelial cells, where it contributes to anti-inflammatory pathways (36–38). Because of its role in the downregulation of the production of proinflammatory

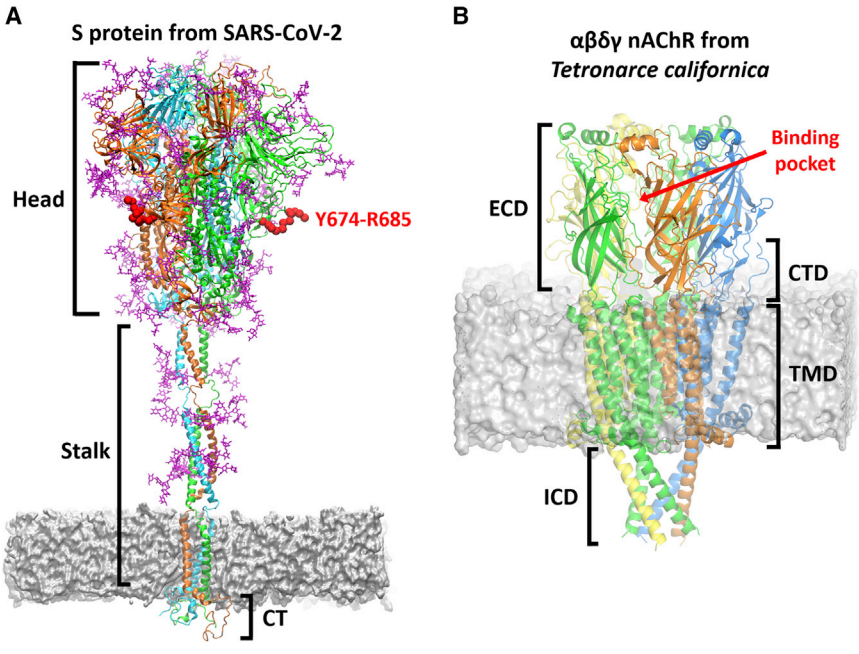

FIGURE 1 Overview of the three-dimensional structures of the SARS-CoV-2 spike protein and the $\alpha\beta\gamma\delta$ nAChR from *T. californica*. (*A*) The model for the complete, fully glycosylated, SARS-CoV-2 spike represents the closed state of the protein after furin cleavage (31). The spike protein is a homotrimer (32); each monomer is shown in different colors, namely green, cyan, and orange, with glycans depicted in pink. Each monomer is formed by three domains: head, stalk, and cytoplasmic tail (CT) (32). The Y674-R685 region is shown in red. (*B*) Shown is the cryoEM structure of the muscle-type receptor from *T. californica* (PDB: 6UWZ) (33). This receptor is a heteropentamer formed of two α- (*green*), one β- (*blue*), one δ- (*yellow*), and one γ- (*orange*) subunits. Each monomer is formed by four domains (28–30): ECD, transmembrane domain (TMD), intracellular domain (ICD), and C-terminal domain (CTD). The agonist binding site is located in the ECDs at the interface between two neighboring subunits. To see this figure in color, go online.

cytokines (36–38), it has been suggested that the α7 nAChR may be involved in the hyperinflammation response that can be caused by SARS-CoV-2 (9,18,24,39). The muscle-type receptor derived from the electric organ of *Tetronarce californica* (formerly *Torpedo californica*) is one of the most extensively studied nAChRs and has provided significant structural insight into this receptor family. It is formed by two α- and one each of β-, δ-, and γ-subunits and has high sequence similarity (55–80% identity) with its human counterpart (40). For this reason and because its structure is available (33), we used it in this work as a proxy for the human muscle-type nAChRs. Muscle fatigue, myalgia, and arthralgia are common symptoms in COVID-19 patients (e.g., (41–43)). However, it is still unclear if these symptoms result from direct muscle damage from viral infection or from the body's inflammatory response (7,41).

According to Changeux et al.'s "nicotinic hypothesis," direct interaction between SARS-CoV-2 and nAChRs occurs via a small region in the viral spike protein (20) (Figs. S3 and S4). The spike is a fusion protein (32,44) found on the surface of the virion that mediates entry into host cells. It is an extensively glycosylated homotrimer, with each monomer formed by three domains (Fig. 1 *A*): head, stalk, and cytoplasmic tail (32). The head comprises two subunits: S1, which binds the ACE2 receptor on host cells (32), and S2, which facilitates membrane fusion (32). The spike contains two proteolytic cleavage sites (32): one ("furin cleavage" site) at the S1/S2 boundary thought to activate the protein (45) and a second in the S2 subunit that releases the fusion peptide (46). The region suggested by Changeux et al. (20) to be directly involved in the interaction with nAChRs spans from Y674 to R685 and is located in the head region of the protein at the interface between the S1 and S2 domains, immediately preceding the S1/S2 cleavage point (32) (Fig. 1 *A*; Figs. S3 and S4). Furin cleaves the peptide bond after R685, thus separating it from its neighbor S686 (e.g., before viral exit from the host cell) (45). Cleavage activation of viral glycoproteins is known to be important for infectivity and virulence (32,45).

The Y674-R685 region contains a four-residue, polybasic PRRA insertion not present in other SARS-CoV-related coronaviruses (47) that is homologous to several neurotoxins known to target nAChRs (20). In SARS-CoV-2, abrogation of the PRRA motif moderately affects virus entry into cells (32,45). This motif has recently been shown experimentally to interact with neuropilin-1 receptors (48), T cell receptors (49), and host cell glycans, such as heparin sulfate (50,51). The high sequence similarities between the Y674-R685 region and several known nAChR antagonists (Fig. S1) suggests that this region of the SARS-CoV-2 spike protein may bind to nAChRs, potentially acting as an antagonist (20). Hence, it has been postulated that nicotine may have an effect in COVID-19 by competing and interfering with this binding. Note that an alternative region (G381 to K386 in the S1 subunit) in the spike protein has been hypothesized to interact with nAChRs (52), but glycosylation makes this unlikely.

Here, we use molecular simulations to examine the "nicotinic hypothesis" proposed by Changeux et al. (20), in particular to test whether the SARS-CoV-2 spike protein can bind stably to nAChRs via the Y674-R685 region and identify interactions that may be involved in the stabilization of the complexes. To test this, we have built structural models for the complexes formed by the 12-residue region from the spike (S-peptide) and the ECDs of three different nAChRs, namely the human $\alpha4\beta2$, human α7, and muscle-like $\alpha\beta\gamma\delta$ receptor from *T. californica* (hereafter named $\alpha\beta\gamma\delta$). These simulations build on our successful previous extensive simulations of nAChRs, which have e.g., identified a general mechanism for signal propagation in this receptor family (53–55) and simulations of the spike (31,56–58) and its interactions (48,59).

RESULTS AND DISCUSSION

Interactions between the SARS-CoV-2 S-peptide and nAChRs

Structural models of the three SARS-CoV-2 S-peptide-nAChR complexes were built based on the cryo-electron microscopy (cryoEM) structure of the $\alpha\beta\gamma\delta$ receptor from *T. californica* with bungarotoxin (33). α-Bungarotoxin is a neurotoxin that acts as a nAChR antagonist, directly competing with acetylcholine (60), and has high sequence similarity with the Y674-R685 region of the spike protein of SARS-CoV-2 (Fig. S1). Twenty models were generated for each complex, and the one with the lowest Modeler objective function (61) (Fig. 2; Fig. S7) was used as the starting point for molecular dynamics (MD) simulations (see the Supporting materials and methods for more details). Three replicate simulations, each 300-ns long, were performed for each complex to investigate the peptide-receptor conformational behavior and possible induced-fit effects.

At the beginning of the simulations, the S-peptide was located in the binding pocket, bound by interactions with both the principal and complementary subunits (Fig. 2; Fig. S7). A close-up view of the peptide-receptor interface reveals extensive contacts (Fig. 2 *B*; Fig. S7 *B*), mainly with the principal subunit. In all three complexes, the side chain of R682 of the S-peptide binds as the recognized positively charged group, a strictly conserved pharmacophore of all nAChR ligands (62,63). As can be seen in Fig. 2 *B*, the guanidinium group of R682 is well positioned inside the aromatic box, forming several cation-π interactions with TyrC1 (α4Y223, α7Y210, and αY214 in the human $\alpha4\beta2$, human α7, and muscle-like $\alpha\beta\gamma\delta$ receptor from *T. californica*, respectively), TyrC2 (α4Y230, α7Y217, and αY222), and TyrA (α4Y126, α7Y115, and αY117). Note that these cation-π interactions do not entirely mimic the binding of nicotine, as no interactions with TrpB are present

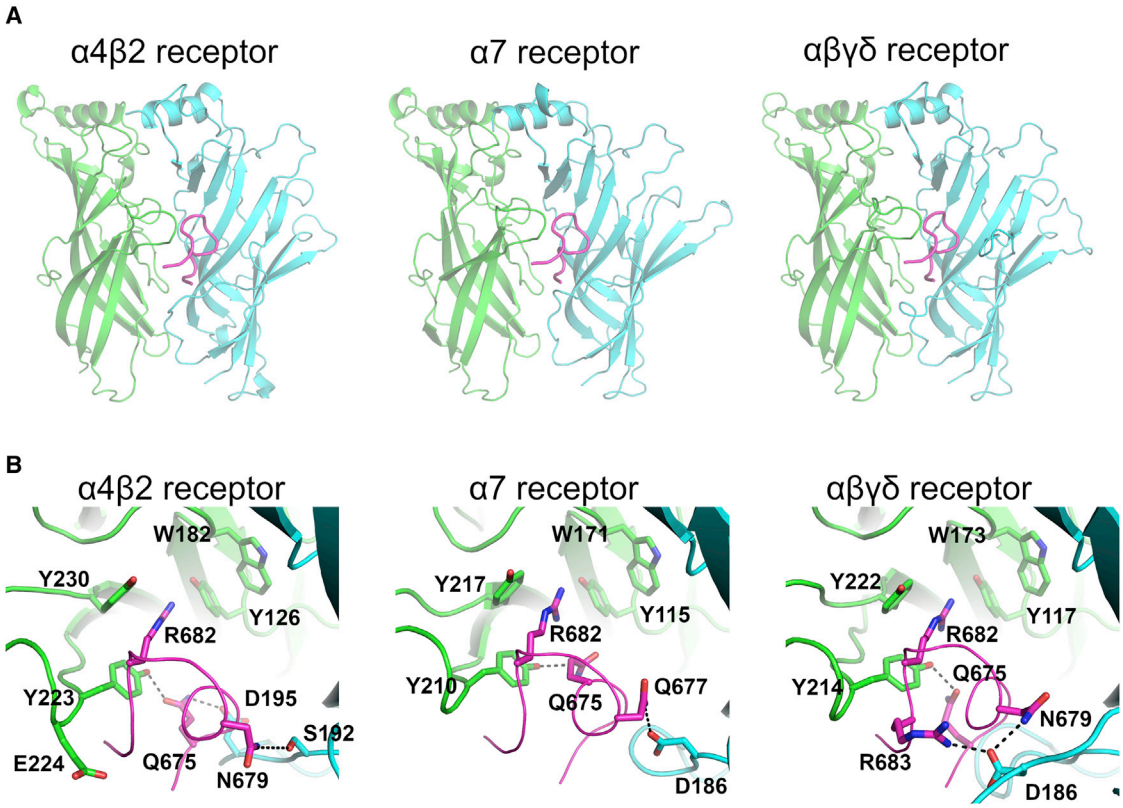

FIGURE 2 **Predicted binding modes of the SARS-CoV-2 S-peptide to different nAChRs. (*A*) Shown are complexes formed by the S-peptide and three different nAChRs, namely the human $\alpha4\beta2$, human $\alpha7$, and the muscle-like $\alpha\beta\gamma\delta$ receptor from *T. californica.* The S-peptide (region Y674-R685) is highlighted in magenta, and the principal and complementary subunits of the receptors are colored in green and cyan, respectively. These models show the conformation of the S-peptide bound to the first pocket at the beginning of the simulations. In the human $\alpha4\beta2$ receptor, the binding pocket is formed by one $\alpha4$ and one $\beta2$ subunit, whereas in the human $\alpha7$ nAChR, the pocket is formed by two $\alpha7$ subunits. In the $\alpha\beta\gamma\delta$ receptor, the two binding pockets are nonequivalent; one is formed by an α and a δ and the second by α- and γ-subunits. (*B*) Shown is a close-up view of the peptide-receptor interaction region. Residues involved in binding of the S-peptide are shown with sticks. Note that the side chain of R682 in the S-peptide is located inside the aromatic box establishing cation-π interactions with some of the highly conserved aromatic residues lining the pocket. Note also that all residue numbers used in this work, unless stated otherwise, refer to the human $\alpha7$ (Uniprot: P36544), human $\alpha4$ (Uniprot: P43681), human $\beta2$ (Uniprot: P17787), *T. californica* α (Uniprot: P02710), *T. californica* δ (Uniprot: P02718), *T. californica* γ (Uniprot: P02714), and SARS-CoV-2 spike protein (Uniprot: P0DTC2) sequences. To see this figure in color, go online.**

(64). R682 is part of the four-residue PRRA insertion not found in other SARS-like coronaviruses (47), and it forms part of the furin cleavage site located at the boundary between the S1 and S2 subunits (32). Additional binding interactions with the peptide are also observed with different residues depending on the receptor subtype; in the $\alpha4\beta2$ nAChR, hydrogen bonds involving the side chains of α4Y223, α4E224, β2S192, and β2D195 in the receptor and Q675, N679, and the main-chain nitrogen of A684 of the S-peptide are observed; in the $\alpha7$ nAChR, two hydrogen bonds between α7D186 and α7Y210 in the receptor and S-peptide Q675 and Q677 are seen; and in the $\alpha\beta\gamma\delta$ receptor from *T. californica*, hydrogen bonds involving αY214 and δD186 from the receptor and Q675, N679, R682, and R683 of the peptide are observed.

The simulations show distinct patterns of dynamical behavior for the S-peptide in the different receptor subtypes. In the $\alpha4\beta2$ and $\alpha7$ complexes, the peptide showed high positional and conformational variability, whereas in the $\alpha\beta\gamma\delta$ complex, it generally remained in the same pose throughout the simulation (Figs. S8 and S10). Similar behavior is observed for the peptides in the two binding pockets in each complex. When bound to the $\alpha4\beta2$ and $\alpha7$ nAChR, the peptide adopted many different binding modes inside the pocket, ranging from highly compact to fully extended conformations (Fig. S10). In contrast, in the $\alpha\beta\gamma\delta$ receptor, the peptide was more compact (Fig. S10). The range of the radius of gyration values for the S-peptide in all three complexes is similar to that observed in the simulations of the full-length glycosylated SARS-CoV-2 spike protein embedded in a viral membrane (Fig. S6; (31)). Principal component analysis (PCA) of the peptide dynamics revealed different conformational behavior of the peptide in the three complexes. When bound to the muscle-like receptor, the peptide shows limited dynamical freedom; it explores a restricted conformational space spanned by the first two principal components (Fig. S11).

The number of hydrogen bonds between the peptide and the receptors over the simulations was determined (Fig. S12). Two more H-bonds are observed in the $\alpha\beta\gamma\delta$ complex than in the $\alpha4\beta2$ and $\alpha7$ receptors (Fig. S12). These additional interactions with the complementary subunit (Fig. S12) probably contribute to the increased stability of this complex and the more compact conformation of the peptide in the $\alpha\beta\gamma\delta$ receptor.

Analysis of the distribution of the distance between the R682 of the peptide and the conserved aromatic residues forming the aromatic box shows the distinctive behavior of the peptide when bound to different receptors (Fig. S13). Interactions with R682, TyrC1, and TyrC2 are quite frequent in all three complexes, being present more than 60% of the time. To examine how deeply into the binding pocket the peptide inserts, we monitored the interactions of R682 with TrpB, a residue lining the back wall of the nAChR aromatic box. TrpB (α4W182, α7W171, and αW173) is highly conserved across the nAChR family, and it makes cation-π and H-bond interactions with the positively charged group on the ligands (62,63). In the $\alpha4\beta2$ and $\alpha\beta\gamma\delta$ complexes, the S-peptide does not extend far into the pocket, and interactions between R682 and TrpB are mostly absent (Fig. S13). In contrast, in the $\alpha7$ complex, the peptide binds more deeply into the hydrophobic cavity, adopting conformations that allow not only for the direct contact between R682 and TrpB (Figs. S14–S15) but also achieve optimal core-binding interactions (Fig. 3). In such configurations, other interactions are present in addition to those with TrpB, namely cation-π interactions with TyrC1 and TyrC2 (Fig. S15). Although no direct contact between R682 and TyrA is observed, both residues are connected through a H-bond network mediated by Q675 from the S-peptide (Fig. S16). This is significant because interactions with TyrA, TrpB, TyrC1, and TyrC2 are known to be critical for ligand binding and to modulate gating in the $\alpha7$ subtype (65–67).

The binding of a ligand or a peptide can be expected to affect the conformational dynamics of the receptors (e.g., (53–55,68–70)). To investigate this, the root mean-square fluctuation (RMSF) profiles of the C_α atoms were determined for all three receptors. Distinct dynamic behaviors are observed for the binding site regions in the different subtypes (Figs. S17–S19). These differences are mostly in loops C and F, two structural motifs important for binding and selectivity (66,71,72). Loop F shows decreased flexibility in the $\alpha4\beta2$ complex, whereas loop C dynamics is more restricted in the muscle-like $\alpha\beta\gamma\delta$ receptor compared with the other two subtypes.

At the beginning of the simulations, in all the three complexes, loop C adopted an open conformation because of the steric interference of the peptide. During the simulations, the $\alpha\beta\gamma\delta$ and $\alpha4\beta2$ receptors mostly maintained this open conformation. In the $\alpha7$ complex, as the peptide moved deeper into the binding pocket, loop C rotated inwards, adopting a semiclosed structure. Loop C capping is known to be important for the anchoring of the ligands in the binding pocket (66,71) and has been suggested to be indirectly involved in gating (54,73). A relationship between loop C position and ligand activation has also been proposed (72); agonists are proposed to stabilize more compact loop conformations, whereas antagonists disfavor loop closing. On this basis, our findings suggest that the S-peptide may act as an antagonist in the $\alpha\beta\gamma\delta$ and $\alpha4\beta2$ receptors, thus inhibiting gating. However, in the $\alpha7$ subtype, it is unclear whether the peptide may be an agonist or antagonist and whether it can promote gating. How the S-peptide affects the different nAChRs may be relevant to understanding COVID-19 pathophysiology (9,18,24,39).

A molecular mechanics Poisson-Boltzmann surface area (MM-PBSA) approach (74,75) was used to calculate the free energy of binding of the S-peptide to the different receptors (Table 1; Table S1). MM-PBSA calculations are an efficient and often useful method to estimate binding free energies (74,75) and are widely used to study protein-ligand interactions in medicinal chemistry (76–78), including in drug design for nAChRs (79,80). The favorable calculated binding energies suggest stable complex

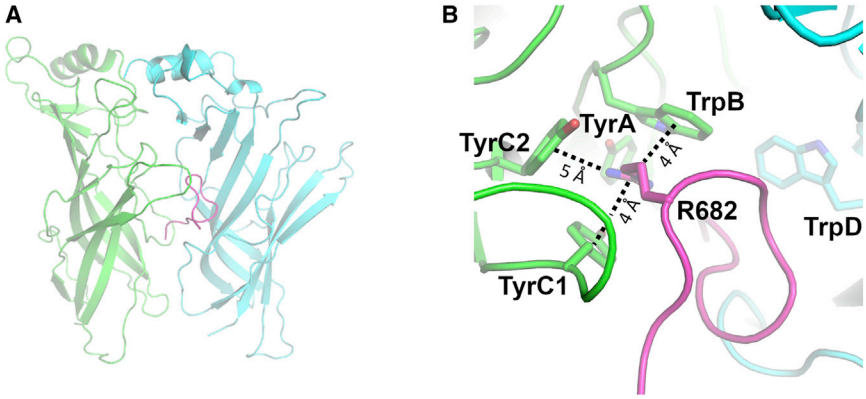

FIGURE 3 Representative conformation of the $\alpha7$ complex, in which direct interaction between TrpB and R682 is observed. (*A*) Shown is an overall view of the S-peptide:$\alpha7$ complex. (*B*) Shown is a close-up view of the R682 interaction region within the aromatic box. The principal and complementary subunits of the $\alpha7$ receptor are colored in green and cyan, respectively. The S-peptide is highlighted in magenta. Interactions between the guanidinium group of R682 and the aromatic rings of TrpB (α7W171), TyrC1 (α7Y210), and TyrC2 (α7Y217) are shown with dashed lines. See also Figs. S13–S16 for more details about the behavior of the S-peptide when bound to $\alpha7$ nAChR. To see this figure in color, go online.

TABLE 1 MM-PBSA relative binding energy values for the S-peptide in the human $\alpha4\beta2$, human $\alpha7$, and muscle-like $\alpha\beta\gamma\delta$ nAChR from *T. californica*

	Average ΔG_{bind} for the complexes (kJ/mol)		
	$\alpha4\beta2$	$\alpha7$	$\alpha\beta\gamma\delta$
First pocket	−215.9 (80.4)	−184.5 (24.3)	−374.3 (98.5)
Second pocket	−215.7 (55.7)	−114.9 (46.6)	−391.5 (75.8)

Numbers in brackets represent the SDs. Note that the values reported in this table are averaged over all replicates (see Table S1 for the ΔG_{bind} for the individual replicates) and do not contain the entropic contribution to the binding energy.

formation between the S-peptide and all three nAChRs (Table 1; Table S1), with different binding affinities depending on the subtype.

In silico alanine-scanning mutagenesis was performed to identify important residues (referred to as "hotspots") in peptide-receptor association (Figs. S20–S22). Hotspots are residues with high energetic contributions to the thermodynamic stability of a given complex (81). Alanine-scanning provides a detailed energy map of a protein-binding interface (81). Here, we used the fast in silico method, BudeAlaScan (81), in which every residue, for both receptor and peptide, is mutated (singly, in turn) to alanine. Hotspots are determined by the difference between the binding free energies of the alanine mutant and wild-type complexes ($\Delta\Delta G_{bind}$) (81). Hotspots were identified at the interface of the receptor, some of them common to all three subtypes (Fig. S23; Tables 2; Table S2). In particular, TyrC1 (α4Y223, α7Y210, and αY214) and the negatively charged residues in the upper part of loop F (β2D195, α7D186, δD201, and δE203) strongly stabilize the complex. In the human $\alpha7$ nAChR, the substitution of several key agonist-binding residues in the aromatic box (namely TyrA (α7Y115), TyrC1 (α7Y210), TrpB (α7W171), and TrpD (α7W77)) by alanine is also predicted to destabilize the interface between the peptide and the receptor. Of the residues in the peptide, Y674, R682, and R685 are the major contributors to stabilizing the interface (Fig. S24). This analysis reinforces the critical role of R682 in binding to nAChRs.

Accessibility of the SARS-CoV-2 S-peptide in MD simulations of the full-length glycosylated spike

Since the beginning of the pandemic, the computational structural biology/biomolecular simulation community has investigated the SARS-CoV-2 spike protein in different states and conditions and the complexes that it forms (e.g., (31,56–59,82–86)). Simulations have revealed the dynamics of the spike and its glycan shield (31,57–59,82,83,85,86) and the effects of the binding of small molecules (56,84). Here, to further explore the "nicotinic hypothesis," we show that the Y674-R685 region (corresponding to the S-peptide) is accessible for binding, using the available MD simulations of the fully glycosylated full-length SARS-CoV-2 spike protein in the open and closed states by Casalino et al. (31). We note that in these models, the Y674-R685 region was modeled de novo as it was entirely (open spike) or partially (closed spike) missing in the initial cryoEM structures (32,44) (for more details, see Supporting materials and methods). In these simulations, the Y674-R685 region adopts conformations potentially compatible with binding to nAChRs (Fig. 4 *A*). Our analysis reveals that the Y674-R685 loop is only weakly shielded by the glycans and is predominantly solvent exposed (Fig. 4; Fig. S5). Especially when the spike is in the closed state (Fig. 4 *B*), the Y674-R685 loop appears highly accessible to a probe with a radius ranging from 1.4 to 15 Å. In contrast, in the open spike (Fig. 4 *C*), a larger variability of the accessible area is observed, preventing an unambiguous interpretation of the glycan shield effect on Y674-R685 for probes with a radius larger than 7 Å. The slightly different and less variable accessibility of the Y674-R585 loop observed in the closed spike when compared the open spike protein is in agreement with the sharper distribution of the radius of gyration calculated for this region in the closed spike (Fig. S6). This behavior might indicate different binding propensity of the S-peptide in the open and closed spike states. We hypothesize that it might be linked to a different packing of the three spike monomers in the two states. We note that the accessibility of this region makes it available to bind other receptors that may also bind the PRRA motif, such as neuropilin-1.

CONCLUSIONS

In summary, the findings reported here support the hypothesis that the SARS-CoV-2 spike protein can interact with nAChRs. Our calculations indicate stable binding of the spike protein to these receptors through a region adjacent to the furin cleavage site and corresponding to the Y674-R685 region. These calculations also show apparent subtype-specific interactions and dynamics for the Y674-R685 region. COVID-19 is known to cause a range of neurological (87,88), muscular (41), and respiratory (89) symptoms, and these predicted interactions may be relevant to understand the pathophysiology associated with this disease.

Our results predict that the Y674-R685 region of the spike protein has affinity for nAChRs. The region in the spike responsible for binding to nAChRs harbors the PRRA motif and shares high sequence similarity with neurotoxins known

TABLE 2 BUDE Alanine-scanning predicted average $\Delta\Delta G_{bind}$ for the hot spots (-3 kJ/mol $\geq$ residue contribution $\leq$ 3 kJ/mol) in the first binding pocket of the receptors

First binding pocket					
$\alpha4\beta2$ receptor		$\alpha7$ receptor		Muscle-like $\alpha\beta\gamma\delta$ receptor	
Residue	$\Delta\Delta G_{bind}$ (kJ/mol)	Residue	$\Delta\Delta G_{bind}$ (kJ/mol)	Residue	$\Delta\Delta G_{bind}$ (kJ/mol)
β2D195	9.5 (3.6)	α7Y210	7.6 (2.2)	αY214	12.1 (2.6)
α4Y223	7.7 (2.0)	α7W77	5.1 (2.0)	δD201	6.1 (1.9)
α4Y230	3.7 (2.2)	α7Y115	3.8 (2.9)	δW197	4.6 (2.3)
β2W32	3.3 (1.7)	α7S188	3.7 (1.9)	δI199	4.0 (0.8)
		α7D186	3.1 (2.1)	δD186	3.9 (1.7)
				δE203	3.8 (2.0)
				αT215	3.1 (1.5)

The average value was calculated over the three replicates. Numbers in brackets represent the SDs (calculated over the 303 frames per complex). Note that the $\Delta\Delta G_{bind}$ corresponds to the difference between mutant and wild-type complexes, and as such, positive $\Delta\Delta G_{bind}$ values mean that the mutation to alanine destabilizes the complex.

to be nAChR antagonists. The guanidinium group of R682 is the key anchoring point to the binding pocket, in which it forms several interactions with the residues that form the aromatic box. Analysis of the structure and dynamics of the full-length glycosylated spike shows that the Y674-R685 region protrudes outside the glycan shield, is solvent accessible (Fig. 4; Fig. S5), and is flexible (Fig. S6), showing that it is accessible to bind to nAChRs (and to other receptors such as neuropilins (48)). Modeling the interaction between the full-length spike and nAChRs indicates that association is possible with the proteins in a nonparallel orientation to one another (Fig. S4). cryoEM and tomography experiments and coarse-grained simulations show considerable bending and tilting of the spike. A tilt angle up to 60° relative to the normal axis of the membrane is observed (57,58,85,90,91). This flexibility of the spike protein would facilitate binding to host nAChRs.

Evidence that the interaction between the Y674-R685 region of the spike and nAChRs is possible comes from the recently characterized interaction of the spike protein with neuropilin-1 (48), which was shown to occur via the same region as the one proposed here. Having explored various possible orientations, we find that only approximately nonparallel arrangements of the spike and receptor allow for their interaction. This nonparallel interaction may not be immediately obvious, but it is consistent with other observations and is possible for two principal reasons: first, membrane curvature and deformation, and second, bending of the stalk of the spike. Experiments (e.g., cryoEM and tomography) and coarse-grained simulations show that a significant degree of stalk bending is possible and that the spike can adopt a wide range of conformations with different degrees of bending (57,85,90,91) given by the three flexible hinges in the spike protein (85).

In the $\alpha4\beta2$ and $\alpha\beta\gamma\delta$ complexes, the conformational dynamics of the bound Y674-R685 peptide are compatible with the hypothesis of it acting as an antagonist; it forces loop C to adopt an open conformation and prevents the formation of important interactions within the binding pocket. Intriguingly, in the $\alpha7$ complexes, the peptide adopts binding modes that allow strong interactions within the aromatic box, raising the question of whether it promotes gating in this subtype. This is important because activation of $\alpha7$ nAChR triggers anti-inflammatory signaling mechanisms in inflammatory cells, leading to a decrease in cytokine production, which may have relevance in understanding early COVID-19 pathology (9,18,24,39). If nicotine does indeed prove to have any clinical value, it is likely that it would be due to interfering with the association with nAChRs. If so, nicotine analogs (e.g., smoking cessation agents such as varenicline (92), cytisine (93), and, potentially, cytisine variants (55)) could also find a useful application for COVID-19.

Given the promising results presented here, structural, mutational, and single-channel studies will be of interest to test the importance of the interactions of the SARS-CoV-2 spike with nAChRs and the potential relevance of these interactions to pathology and infectivity in COVID-19. To assist with further investigations, we make our simulation files and datasets available and openly accessible, in accordance with the sharing principles agreed to by our community for simulations relevant to COVID-19 (94).

SUPPORTING MATERIAL

Supporting Material can be found online at https://doi.org/10.1016/j.bpj.2021.01.037.

AUTHOR CONTRIBUTIONS

Conceptualization/design of the work: A.S.F.O. and A.J.M. Acquisition and analysis of the data: A.S.F.O., A.A.I., L.C., and Z.G. Writing of the manuscript: A.S.F.O., A.A.I., L.C., and A.J.M. Review and editing of the manuscript: A.S.F.O., A.J.M., I.B., Z.G., T.G., D.K.S., R.B.S., and R.E.A. Funding acquisition: T.M., R.E.A., and A.J.M.

ACKNOWLEDGMENTS

A.J.M. and A.S.F.O. thank EPSRC (grant EP/M022609/1) and the Elizabeth Blackwell Institute for Health Research, University of Bristol for financial

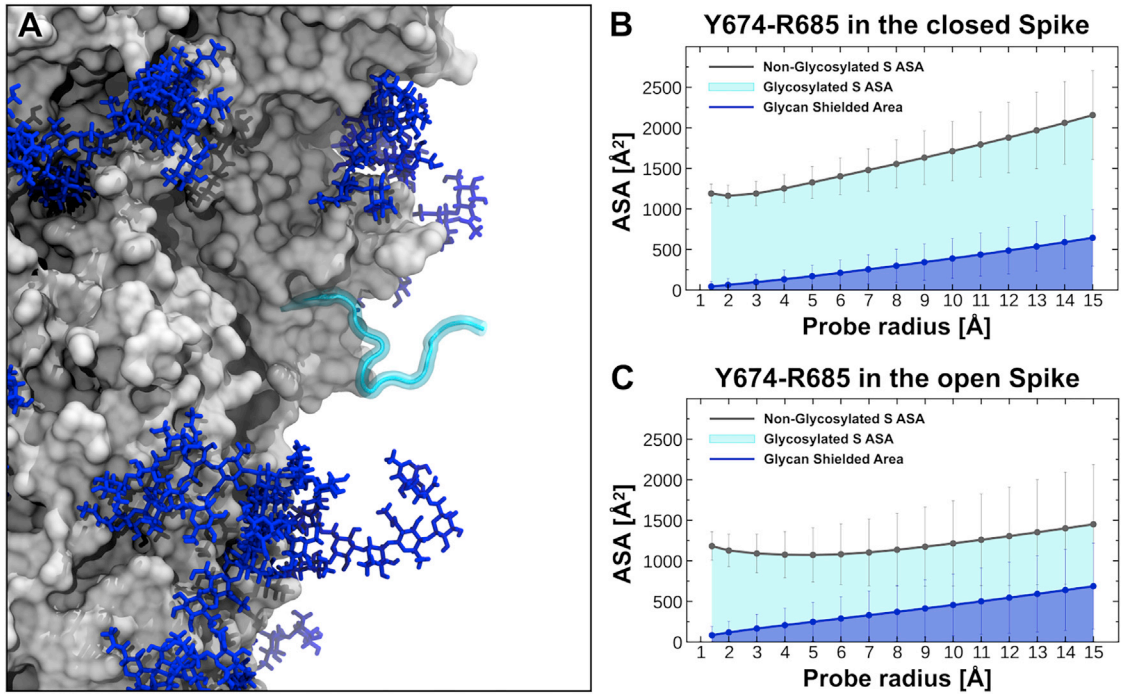

FIGURE 4 Accessible surface area (ASA) of Y674-R685 region in the context of the fully glycosylated full-length SARS-CoV-2 spike. (*A*) Shown is a snapshot taken from the simulations by Casalino et al. (31) of the glycosylated full-length SARS-CoV-2 spike in the closed state showing Y674-R685 loop protruding into the solvent. The protein is depicted with a gray surface, whereas 674–685 loop is shown as a cyan ribbon. The glycans are illustrated with blue sticks. (*B–C*) The ASA of the of residues 674–685 (corresponding to the S-peptide) and the area shielded by glycans at multiple probe radii from 1.4 Å (water molecule) to 15 Å are calculated using the available MD trajectories of the full-length models of the glycosylated SARS-CoV-2 spike protein in the closed (*B*) and open states (*C*) from Casalino et al. (31). The area of 674–685 shielded by the glycans is presented in blue, whereas the gray line represents the accessible area of 674–685 in the absence of glycans. Highlighted in cyan is the area of 674–685 that remains accessible in the presence of glycans. The calculated values have been averaged across the three chains and across the different replicas performed for each system by Casalino et al. (31). Error bars correspond to ± SD. To see this figure in color, go online.

support (Elizabeth Blackwell Institute Rapid Response Funding Call (COVID-19)). MD simulations were carried out using the computational facilities of the Advanced Computing Research Centre, University of Bristol (http://www.bris.ac.uk/acrc) and using Oracle Public Cloud Infrastructure (https://cloud.oracle.com/en_US/iaas) under an award for COVID-19 research. We thank Drs. Simon Bennie and Jonathan Barnoud for help with the Cluster-in-the-cloud and the creation of a scalable cluster on the Oracle Cloud. A.J.M., A.S.F.O., R.B.S., and D.K.S. also thank EPSRC for provision of ARCHER HPC time through HECBioSim (HECBioSim.ac.uk) under a COVID-19 award. R.E.A. acknowledges support from NIH (GM132826), NSF RAPID (MCB-2032054), an award from the RCSA Research Corp., and a UC San Diego Moore's Cancer Center 2020 SARS-COV-2 seed grant. R.E.A., L.C., and Z.G. thank the Texas Advanced Computing Center (TACC) Frontera team and acknowledge computer time made available through a Director's Discretionary Allocation (made possible by the NSF award OAC-1818253).

SUPPORTING CITATIONS

References (95–123) appear in the Supporting material.

REFERENCES

1. Yan, R., Y. Zhang, …, Q. Zhou. 2020. Structural basis for the recognition of SARS-CoV-2 by full-length human ACE2. *Science.* 367:1444–1448.
2. Rothan, H. A., and S. N. Byrareddy. 2020. The epidemiology and pathogenesis of coronavirus disease (COVID-19) outbreak. *J. Autoimmun.* 109:102433.
3. Lake, M. A. 2020. What we know so far: COVID-19 current clinical knowledge and research. *Clin. Med. (Lond.).* 20:124–127.
4. Puntmann, V. O., M. L. Carerj, …, E. Nagel. 2020. Outcomes of cardiovascular magnetic resonance imaging in patients recently recovered from coronavirus disease 2019 (COVID-19). *JAMA Cardiol.* 5:1265–1273.
5. Varga, Z., A. J. Flammer, …, H. Moch. 2020. Endothelial cell infection and endotheliitis in COVID-19. *Lancet.* 395:1417–1418.
6. Puelles, V. G., M. Lütgehetmann, …, T. B. Huber. 2020. Multiorgan and renal tropism of SARS-CoV-2. *N. Engl. J. Med.* 383:590–592.
7. Zhang, Y., X. Geng, …, H. Wang. 2020. New understanding of the damage of SARS-CoV-2 infection outside the respiratory system. *Biomed. Pharmacother.* 127:110195.
8. Desforges, M., A. Le Coupanec, …, P. J. Talbot. 2019. Human coronaviruses and other respiratory viruses: underestimated opportunistic pathogens of the central nervous system? *Viruses.* 12:1–28.
9. Tizabi, Y., B. Getachew, …, M. Aschner. 2020. Nicotine and the nicotinic cholinergic system in COVID-19. *FEBS J.* 287:3656–3663.
10. Baig, A. M., A. Khaleeq, …, H. Syeda. 2020. Evidence of the COVID-19 virus targeting the CNS: tissue distribution, host-virus interaction, and proposed neurotropic mechanisms. *ACS Chem. Neurosci.* 11:995–998.
11. Baig, A. M., and E. C. Sanders. 2020. Heralding healthcare professionals: recognition of neurological deficits in COVID-19. *ACS Chem. Neurosci.* 11:1701–1703.

12. Alam, S. B., S. Willows, …, J. K. Sandhu. 2020. Severe acute respiratory syndrome coronavirus 2 may be an underappreciated pathogen of the central nervous system. *Eur. J. Neurol.* 27:2348–2360.
13. Dong, E., H. Du, and L. Gardner. 2020. An interactive web-based dashboard to track COVID-19 in real time. *Lancet Infect. Dis.* 20:533–534.
14. Huang, C., Y. Wang, …, B. Cao. 2020. Clinical features of patients infected with 2019 novel coronavirus in Wuhan, China. *Lancet.* 395:497–506.
15. Farsalinos, K., A. Barbouni, and R. Niaura. 2020. Systematic review of the prevalence of current smoking among hospitalized COVID-19 patients in China: could nicotine be a therapeutic option? *Intern. Emerg. Med.* 15:845–852.
16. Guan, W. J., Z. Y. Ni, …, N. S. Zhong; China Medical Treatment Expert Group for Covid-19. 2020. Clinical characteristics of coronavirus Disease 2019 in China. *N. Engl. J. Med.* 382:1708–1720.
17. Liu, W., Z. W. Tao, …, Y. Hu. 2020. Analysis of factors associated with disease outcomes in hospitalized patients with 2019 novel coronavirus disease. *Chin. Med. J. (Engl.).* 133:1032–1038.
18. Gonzalez-Rubio, J., C. Navarro-Lopez, …, A. Najera. 2020. Cytokine release syndrome (CRS) and nicotine in COVID-19 patients: trying to calm the storm. *Front. Immunol.* 11:1359.
19. Cohen, B., A. Nichols, …, H. Lester. 2020. Successful cessation programs that reduce comorbidity may explain surprisingly low smoking rates among hospitalized COVID-19 patients. *Qeios* https://doi.org/10.32388/WURFH0.
20. Changeux, J. P., Z. Amoura, …, M. Miyara. 2020. A nicotinic hypothesis for Covid-19 with preventive and therapeutic implications. *C. R. Biol.* 343:33–39.
21. Altable Pérez, M., and J. M. De la Serna. 2020. Neuroinvasion and viral reservoir in COVID-19. *Cureus.* 12:e11014.
22. De Virgiliis, F., and S. Di Giovanni. 2020. Lung innervation in the eye of a cytokine storm: neuroimmune interactions and COVID-19. *Nat. Rev. Neurol.* 16:645–652.
23. Leitzke, M., D. Stefanovic, …, P. Schönknecht. 2020. Autonomic balance determines the severity of COVID-19 courses. *Bioelectron. Med.* 6:22.
24. Dratcu, L., and X. Boland. 2020. Does nicotine prevent cytokine storms in COVID19? *Cureus.* 12:e11220.
25. Wonnacott, S. 1997. Presynaptic nicotinic ACh receptors. *Trends Neurosci.* 20:92–98.
26. Gharpure, A., C. M. Noviello, and R. E. Hibbs. 2020. Progress in nicotinic receptor structural biology. *Neuropharmacology.* 171:108086.
27. Cecchini, M., and J. P. Changeux. 2015. The nicotinic acetylcholine receptor and its prokaryotic homologues: structure, conformational transitions & allosteric modulation. *Neuropharmacology.* 96:137–149.
28. Thompson, A. J., H. A. Lester, and S. C. Lummis. 2010. The structural basis of function in Cys-loop receptors. *Q. Rev. Biophys.* 43:449–499.
29. Nemecz, Á., M. S. Prevost, …, P. J. Corringer. 2016. Emerging molecular mechanisms of signal transduction in pentameric ligand-gated ion channels. *Neuron.* 90:452–470.
30. Changeux, J. P. 2018. The nicotinic acetylcholine receptor: a typical 'allosteric machine'. *Philos. Trans. R. Soc. Lond. B Biol. Sci.* 373:20170174.
31. Casalino, L., Z. Gaieb, …, R. E. Amaro. 2020. Beyond shielding: the roles of glycans in the SARS-CoV-2 spike protein. *ACS Cent. Sci.* 6:1722–1734.
32. Walls, A. C., Y. J. Park, …, D. Veesler. 2020. Structure, function, and antigenicity of the SARS-CoV-2 spike glycoprotein. *Cell.* 181:281–292.e6.
33. Rahman, M. M., J. Teng, …, R. E. Hibbs. 2020. Structure of the native muscle-type nicotinic receptor and inhibition by snake venom toxins. *Neuron.* 106:952–962.e5.
34. Dineley, K. T., A. A. Pandya, and J. L. Yakel. 2015. Nicotinic ACh receptors as therapeutic targets in CNS disorders. *Trends Pharmacol. Sci.* 36:96–108.
35. Haydar, S. N., and J. Dunlop. 2010. Neuronal nicotinic acetylcholine receptors - targets for the development of drugs to treat cognitive impairment associated with schizophrenia and Alzheimer's disease. *Curr. Top. Med. Chem.* 10:144–152.
36. Martelli, D., D. G. Farmer, and S. T. Yao. 2016. The splanchnic anti-inflammatory pathway: could it be the efferent arm of the inflammatory reflex? *Exp. Physiol.* 101:1245–1252.
37. Tracey, K. J. 2002. The inflammatory reflex. *Nature.* 420:853–859.
38. Maturo, M. G., M. Soligo, …, C. Nardini. 2019. The greater inflammatory pathway-high clinical potential by innovative predictive, preventive, and personalized medical approach. *EPMA J.* 11:1–16.
39. Manni, L., P. Tieri, and M. Soligo. 2020. A contribution to the hypothesis of nicotinic challenge as therapeutic option for COVID-19 patients. *Qeios* https://doi.org/10.32388/UJX3KN.2.
40. Unwin, N. 2013. Nicotinic acetylcholine receptor and the structural basis of neuromuscular transmission: insights from Torpedo postsynaptic membranes. *Q. Rev. Biophys.* 46:283–322.
41. Cipollaro, L., L. Giordano, …, N. Maffulli. 2020. Musculoskeletal symptoms in SARS-CoV-2 (COVID-19) patients. *J. Orthop. Surg. Res.* 15:178.
42. Goyal, P., J. J. Choi, …, M. M. Safford. 2020. Clinical characteristics of Covid-19 in New York city. *N. Engl. J. Med.* 382:2372–2374.
43. Vetter, P., D. L. Vu, …, F. Jacquerioz. 2020. Clinical features of covid-19. *BMJ.* 369:m1470.
44. Wrapp, D., N. Wang, …, J. S. McLellan. 2020. Cryo-EM structure of the 2019-nCoV spike in the prefusion conformation. *Science.* 367:1260–1263.
45. Davidson, A. D., M. K. Williamson, …, D. A. Matthews. 2020. Characterisation of the transcriptome and proteome of SARS-CoV-2 reveals a cell passage induced in-frame deletion of the furin-like cleavage site from the spike glycoprotein. *Genome Med.* 12:68.
46. Apellániz, B., N. Huarte, …, J. Nieva. 2014. The three lives of viral fusion peptides. *Chem Phys Lipids.* 181:40–55.
47. Hoffmann, M., H. Kleine-Weber, and S. Pöhlmann. 2020. A multibasic cleavage site in the spike protein of SARS-CoV-2 is essential for infection of human lung cells. *Mol. Cell.* 78:779–784.e5.
48. Daly, J. L., B. Simonetti, …, Y. Yamauchi. 2020. Neuropilin-1 is a host factor for SARS-CoV-2 infection. *Science.* 370:861–865.
49. Cheng, M. H., S. Zhang, …, I. Bahar. 2020. Superantigenic character of an insert unique to SARS-CoV-2 spike supported by skewed TCR repertoire in patients with hyperinflammation. *Proc. Natl. Acad. Sci. USA.* 117:25254–25262.
50. Zhang, Q., C. Z. Chen, …, Y. Ye. 2020. Heparan sulfate assists SARS-CoV-2 in cell entry and can be targeted by approved drugs in vitro. *Cell Discov.* 6:80.
51. Clausen, T. M., D. R. Sandoval, …, J. D. Esko. 2020. SARS-CoV-2 infection depends on cellular heparan sulfate and ACE2. *Cell.* 183:1043–1057.e15.
52. Farsalinos, K., E. Eliopoulos, …, K. Poulas. 2020. Nicotinic cholinergic system and COVID-19: in silico identification of an interaction between SARS-CoV-2 and nicotinic receptors with potential therapeutic targeting implications. *Int. J. Mol. Sci.* 21:5807.
53. Oliveira, A. S. F., D. K. Shoemark, …, A. J. Mulholland. 2019. Identification of the initial steps in signal transduction in the $\alpha 4\beta 2$ nicotinic receptor: insights from equilibrium and nonequilibrium simulations. *Structure.* 27:1171–1183.e3.
54. Oliveira, A. S. F., C. J. Edsall, …, A. J. Mulholland. 2019. A general mechanism for signal propagation in the nicotinic acetylcholine receptor family. *J. Am. Chem. Soc.* 141:19953–19958.
55. Campello, H. R., S. G. Del Villar, …, T. Gallagher. 2018. Unlocking nicotinic selectivity via direct C–H functionalisation of (–)-cytisine. *Chem.* 4:1710–1725.

56. Toelzer, C., K. Gupta, …, C. Schaffitzel. 2020. Free fatty acid binding pocket in the locked structure of SARS-CoV-2 spike protein. *Science.* 370:725–730.

57. Casalino, L., A. Dommer, …, R. E. Amaro. 2020. AI-driven multiscale simulations illuminate mechanisms of SARS-CoV-2 spike dynamics. *bioRxiv* https://doi.org/10.1101/2020.11.19.390187.

58. Yu, A., A. J. Pak, …, G. A. Voth. 2020. A multiscale coarse-grained model of the SARS-CoV-2 virion. *Biophys. J.* 120:1–8.

59. Barros, E. P., L. Casalino, …, R. E. Amaro. 2020. The flexibility of ACE2 in the context of SARS-CoV-2 infection. *Biophys. J.* 120:1–13.

60. Wang, G. K., and J. Schmidt. 1980. Primary structure and binding properties of iodinated derivatives of alpha-bungarotoxin. *J. Biol. Chem.* 255:11156–11162.

61. Sali, A. 1995. Comparative protein modeling by satisfaction of spatial restraints. *Mol. Med. Today.* 1:270–277.

62. Dougherty, D. A. 2008. Cys-loop neuroreceptors: structure to the rescue? *Chem. Rev.* 108:1642–1653.

63. Corringer, P. J., F. Poitevin, …, J. P. Changeux. 2012. Structure and pharmacology of pentameric receptor channels: from bacteria to brain. *Structure.* 20:941–956.

64. Morales-Perez, C. L., C. M. Noviello, and R. E. Hibbs. 2016. X-ray structure of the human $\alpha4\beta2$ nicotinic receptor. *Nature.* 538:411–415.

65. Williams, D. K., C. Stokes, …, R. L. Papke. 2009. Differential regulation of receptor activation and agonist selectivity by highly conserved tryptophans in the nicotinic acetylcholine receptor binding site. *J. Pharmacol. Exp. Ther.* 330:40–53.

66. Puskar, N. L., X. Xiu, …, D. A. Dougherty. 2011. Two neuronal nicotinic acetylcholine receptors, alpha4beta4 and alpha7, show differential agonist binding modes. *J. Biol. Chem.* 286:14618–14627.

67. Van Arnam, E. B., E. E. Blythe, …, D. A. Dougherty. 2013. An unusual pattern of ligand-receptor interactions for the $\alpha7$ nicotinic acetylcholine receptor, with implications for the binding of varenicline. *Mol. Pharmacol.* 84:201–207.

68. Suresh, A., and A. Hung. 2016. Molecular simulation study of the unbinding of α-conotoxin [ϒ4E]GID at the $\alpha7$ and $\alpha4\beta2$ neuronal nicotinic acetylcholine receptors. *J. Mol. Graph. Model.* 70:109–121.

69. Grazioso, G., J. Sgrignani, …, A. Cavalli. 2015. Allosteric modulation of alpha7 nicotinic receptors: mechanistic insight through metadynamics and essential dynamics. *J. Chem. Inf. Model.* 55:2528–2539.

70. Arias, H. R., D. Feuerbach, and M. Ortells. 2015. Functional and structural interaction of (-)-lobeline with human $\alpha4\beta2$ and $\alpha4\beta4$ nicotinic acetylcholine receptor subtypes. *Int. J. Biochem. Cell Biol.* 64:15–24.

71. Horenstein, N. A., T. J. McCormack, …, R. L. Papke. 2007. Reversal of agonist selectivity by mutations of conserved amino acids in the binding site of nicotinic acetylcholine receptors. *J. Biol. Chem.* 282:5899–5909.

72. Nys, M., D. Kesters, and C. Ulens. 2013. Structural insights into Cys-loop receptor function and ligand recognition. *Biochem. Pharmacol.* 86:1042–1053.

73. Purohit, P., and A. Auerbach. 2013. Loop C and the mechanism of acetylcholine receptor-channel gating. *J. Gen. Physiol.* 141:467–478.

74. Wang, C., D. Greene, …, R. Luo. 2018. Recent developments and applications of the MMPBSA method. *Front. Mol. Biosci.* 4:87.

75. Genheden, S., and U. Ryde. 2015. The MM/PBSA and MM/GBSA methods to estimate ligand-binding affinities. *Expert Opin. Drug Discov.* 10:449–461.

76. Slynko, I., K. Schmidtkunz, …, W. Sippl. 2016. Identification of highly potent protein kinase C-related kinase 1 inhibitors by virtual screening, binding free energy rescoring, and in vitro testing. *ChemMedChem.* 11:2084–2094.

77. Evers, A., and T. Klabunde. 2005. Structure-based drug discovery using GPCR homology modeling: successful virtual screening for antagonists of the alpha1A adrenergic receptor. *J. Med. Chem.* 48:1088–1097.

78. Raza, S., K. E. Ranaghan, …, S. S. Azam. 2019. Visualizing protein-ligand binding with chemical energy-wise decomposition (CHEWD): application to ligand binding in the kallikrein-8 S1 Site. *J. Comput. Aided Mol. Des.* 33:461–475.

79. Grazioso, G., D. Y. Pomè, …, M. De Amici. 2009. Design of novel alpha7-subtype-preferring nicotinic acetylcholine receptor agonists: application of docking and MM-PBSA computational approaches, synthetic and pharmacological studies. *Bioorg. Med. Chem. Lett.* 19:6353–6357.

80. Grazioso, G., A. Cavalli, …, C. De Micheli. 2008. Alpha7 nicotinic acetylcholine receptor agonists: prediction of their binding affinity through a molecular mechanics Poisson-Boltzmann surface area approach. *J. Comput. Chem.* 29:2593–2602.

81. Ibarra, A. A., G. J. Bartlett, …, A. J. Wilson. 2019. Predicting and experimentally validating hot-spot residues at protein-protein interfaces. *ACS Chem. Biol.* 14:2252–2263.

82. Sikora, M., S. v. Bulow, …, G. Hummer. 2020. Map of SARS-CoV-2 spike epitopes not shielded by glycans. *bioRxiv* https://doi.org/10.1101/2020.07.03.186825.

83. Zimmerman, M. I., J. Porter, …, G. R. Bowman. 2020. SARS-CoV-2 simulations go exascale to capture spike opening and reveal cryptic pockets across the proteome. *bioRxiv* https://doi.org/10.1101/2020.06.27.175430.

84. Shoemark, D., C. Colenso, …, A. Mulholland. 2020. Molecular simulations suggest vitamins, retinoids and steroids as ligands binding the free fatty acid pocket of SARS-CoV-2 spike protein. *ChemRxiv* https://doi.org/10.26434/chemrxiv.13143761.v1.

85. Turoňová, B., M. Sikora, …, M. Beck. 2020. In situ structural analysis of SARS-CoV-2 spike reveals flexibility mediated by three hinges. *Science.* 370:203–208.

86. Fallon, L., K. Belfon, …, C. Simmerling. 2020. Free energy landscapes for RBD opening in SARS-CoV-2 spike glycoprotein simulations suggest key interactions and a potentially druggable allosteric pocket. *ChemRxiv* https://doi.org/10.26434/chemrxiv.13502646.v1.

87. Ellul, M. A., L. Benjamin, …, T. Solomon. 2020. Neurological associations of COVID-19. *Lancet Neurol.* 19:767–783.

88. Paterson, R. W., R. L. Brown, …, M. S. Zandi. 2020. The emerging spectrum of COVID-19 neurology: clinical, radiological and laboratory findings. *Brain.* 143:3104–3120.

89. Yuki, K., M. Fujiogi, and S. Koutsogiannaki. 2020. COVID-19 pathophysiology: a review. *Clin. Immunol.* 215:108427.

90. Yao, H., Y. Song, …, S. Li. 2020. Molecular architecture of the SARS-CoV-2 virus. *Cell.* 183:730–738.e13.

91. Ke, Z., J. Oton, …, J. A. G. Briggs. 2020. Structures and distributions of SARS-CoV-2 spike proteins on intact virions. *Nature.* 588:498–502.

92. Hays, J. T., and J. O. Ebbert. 2008. Varenicline for tobacco dependence. *N. Engl. J. Med.* 359:2018–2024.

93. Etter, J. F. 2006. Cytisine for smoking cessation: a literature review and a meta-analysis. *Arch. Intern. Med.* 166:1553–1559.

94. Amaro, R. E., and A. J. Mulholland. 2020. A community letter regarding sharing biomolecular simulation data for COVID-19. *J. Chem. Inf. Model.* 60:2653–2656.

95. Walsh, R. M., Jr., S. H. Roh, …, R. E. Hibbs. 2018. Structural principles of distinct assemblies of the human $\alpha4\beta2$ nicotinic receptor. *Nature.* 557:261–265.

96. Lester, H. A. 1972. Blockade of acetylcholine receptors by cobra toxin: electrophysiological studies. *Mol. Pharmacol.* 8:623–631.

97. Bateman, A., M. Martin, …, U. Consortium; The UniProt Consortium. 2017. UniProt: the universal protein knowledgebase. *Nucleic Acids Res.* 45:D158–D169.

98. McWilliam, H., W. Li, …, R. Lopez. 2013. Analysis tool web services from the EMBL-EBI. *Nucleic Acids Res.* 41:W597–W600.

99. Sievers, F., and D. G. Higgins. 2018. Clustal Omega for making accurate alignments of many protein sequences. *Protein Sci.* 27:135–145.

100. Sali, A., L. Potterton, …, M. Karplus. 1995. Evaluation of comparative protein modeling by MODELLER. *Proteins.* 23:318–326.

101. Laskowski, R. A., M. W. Macarthur, …, J. M. Thornton. 1993. Procheck - a program to check the stereochemical quality of protein structures. *J. Appl. Cryst.* 26:283–291.

102. Søndergaard, C. R., M. H. Olsson, …, J. H. Jensen. 2011. Improved treatment of ligands and coupling effects in empirical calculation and rationalization of pKa values. *J. Chem. Theory Comput.* 7:2284–2295.

103. Olsson, M. H., C. R. Søndergaard, …, J. H. Jensen. 2011. PROPKA3: consistent treatment of internal and surface residues in empirical pKa predictions. *J. Chem. Theory Comput.* 7:525–537.

104. Jorgensen, W. L., J. Chandrasekhar, …, M. L. Klein. 1983. Comparison of simple potential functions for simulating liquid water. *J. Chem. Phys.* 79:926–935.

105. Lindorff-Larsen, K., S. Piana, …, D. E. Shaw. 2010. Improved side-chain torsion potentials for the Amber ff99SB protein force field. *Proteins.* 78:1950–1958.

106. Bussi, G., D. Donadio, and M. Parrinello. 2007. Canonical sampling through velocity rescaling. *J. Chem. Phys.* 126:014101.

107. Parrinello, M., and A. Rahman. 1981. Polymorphic transitions in single crystals: a new molecular dynamics method. *J. Appl. Phys.* 52:7182–7190.

108. Nosé, S., and M. L. Klein. 1983. Constant pressure molecular dynamics for molecular systems. *Mol. Phys.* 50:1055–1076.

109. Essmann, U., L. Perera, and M. L. Berkowitz. 1995. A smooth particle mesh Ewald method. *J. Chem. Phys.* 103:8577–8593.

110. Allen, M. P., and D. J. Tildesley. 1987. Computer simulation of liquids.. Clarendon Press, Oxford, UK.

111. Abraham, M. J., T. Murtola, …, E. Lindahl. 2015. GROMACS: high performance molecular simulations through multi-level parallelism from laptops to supercomputers. *SoftwareX.* 2:19–25.

112. Delano, W. L. 2003. The Pymol molecular graphics system. version 0.98. Delano Scientific LLC, San Carlos, CA.

113. DeLano, W. L. 2009. PyMOL molecular viewer: updates and refinements. Abstracts of Papers of the American Chemical Society.

114. Ng, H. W., C. A. Laughton, and S. W. Doughty. 2013. Molecular dynamics simulations of the adenosine A2a receptor: structural stability, sampling, and convergence. *J. Chem. Inf. Model.* 53:1168–1178.

115. Kumari, R., R. Kumar, A. Lynn; Open Source Drug Discovery Consortium. 2014. g_mmpbsa–a GROMACS tool for high-throughput MM-PBSA calculations. *J. Chem. Inf. Model.* 54:1951–1962.

116. Baker, N. A., D. Sept, …, J. A. McCammon. 2001. Electrostatics of nanosystems: application to microtubules and the ribosome. *Proc. Natl. Acad. Sci. USA.* 98:10037–10041.

117. Wood, C. W., A. A. Ibarra, …, R. B. Sessions. 2020. BAlaS: fast, interactive and accessible computational alanine-scanning using BudeAlaScan. *Bioinformatics.* 36:2917–2919.

118. Wood, C. W., J. W. Heal, …, D. N. Woolfson. 2017. ISAMBARD: an open-source computational environment for biomolecular analysis, modelling and design. *Bioinformatics.* 33:3043–3050.

119. McIntosh-Smith, S., J. Price, …, A. A. Ibarra. 2015. High performance *in silico* virtual drug screening on many-core processors. *Int. J. High Perform. Comput. Appl.* 29:119–134.

120. Lentz, T. L., T. G. Burrage, …, G. H. Tignor. 1982. Is the acetylcholine receptor a rabies virus receptor? *Science.* 215:182–184.

121. Hueffer, K., S. Khatri, …, M. K. Schulte. 2017. Rabies virus modifies host behaviour through a snake-toxin like region of its glycoprotein that inhibits neurotransmitter receptors in the CNS. *Sci. Rep.* 7:12818.

122. Donnelly-Roberts, D. L., and T. L. Lentz. 1989. Synthetic peptides of neurotoxins and rabies virus glycoprotein behave as antagonists in a functional assay for the acetylcholine receptor. *Pept. Res.* 2:221–226.

123. Lan, J., J. Ge, …, X. Wang. 2020. Structure of the SARS-CoV-2 spike receptor-binding domain bound to the ACE2 receptor. *Nature.* 581:215–220.

Biophysical Journal, Volume *120*

Supplemental information

A potential interaction between the SARS-CoV-2 spike protein and nicotinic acetylcholine receptors

A. Sofia F. Oliveira, Amaurys Avila Ibarra, Isabel Bermudez, Lorenzo Casalino, Zied Gaieb, Deborah K. Shoemark, Timothy Gallagher, Richard B. Sessions, Rommie E. Amaro, and Adrian J. Mulholland

Supporting Information

A potential interaction between the SARS-CoV-2 spike protein and nicotinic receptors

A. Sofia F. Oliveira, Amaurys Avila Ibarra, Isabel Bermudez, Lorenzo Casalino, Zied Gaieb, Deborah K. Shoemark, Timothy Gallagher, Richard B. Sessions, Rommie E. Amaro and Adrian J. Mulholland

Table of Contents

Materials and methods

Modelling the interaction between nAChR and Y674-R685 from the spike protein

The structural models for the complexes formed by the extracellular domains of the human α7, human α4β2 and muscle-like αβγδ nAChR from *Tetronarce californica* and the Y674-R685 region from SARS-CoV-2 (hereafter named as the S-peptide) were constructed using the cryoEM structure of the αβγδ receptor from *Tetronarce californica* (formerly *Torpedo californica*) with α-bungarotoxin (1) (PDB code: 6UWZ) as a template. Note that we constructed the homology model for the ECDs of human α7 nAChR because there is no X-ray or cryoEM structure for this nAChR subtype in the Protein Data Bank. Note also that the experimentally determined structures available for the human α4β2 nAChR (2, 3) have nicotine bound in the binding pockets and as such show loop C in a closed 'capped' conformation. Loop C acts as a binding pocket lid, and it adapts its shape to the size of the ligands (4, 5). Given that there is no experimental structure for this subtype with loop C in the open 'uncapped' conformation, a homology model was built for the ECDs of human α4β2 nAChR based on the cryoEM structure of the αβγδ receptor with an antagonist (α-bungarotoxin) bound (1).

The structure used here as template reflects the closed state of the muscle-type αβγδ nAChR stabilized by the binding of the two α-bungarotoxin molecules at the α-γ and α-δ interfaces (1). α-bungarotoxin is a 74-residue neurotoxin that binds to the muscle receptors in an (almost) irreversible way (6), and it acts as an antagonist, directly competing with acetylcholine (4, 5). The binding of α-bungarotoxin to neuromuscular junction receptors induces paralysis, respiratory failure, and eventually death (7). The sequence alignment between the S-peptide and α-bungarotoxin was taken from the work of Changeux *et al*. (8). The sequences for the different nAChR subunits were obtained from the UniProt database (9): human α7 (UniProt code P36544), human α4 (UniProt code P43681), human β2 (UniProt code P17787) and aligned with the template using Clustal Omega (10, 11). Twenty models were generated for each complex using Modeller 9v20 (12, 13). The best model for each complex (the one with the lowest value for Modeller's objective function (13)) was further analysed using Procheck (14). Overall, the α4β2 and α7 models are similar to the structures used by us in previous work (15, 16), with the exception of the loop C region that shows an open, uncapped, conformation and loop F that was slightly displaced to accommodate the S-peptide.

MD simulations

The best model for each complex was used as the starting point for the molecular dynamics (MD) simulations. Three systems were prepared, the human α7, human α4β2 and αβγδ nAChR from *Tetronarce californica,* each with two SARS-CoV-2 S-peptides bound, one in each nonconsecutive binding pocket. The protonation state of each titratable residue in the receptor and peptides at pH 7.0

was determined using PROPKA (17, 18). All systems were solvated using TIP3P water molecules (19), and an ionic concentration of 0.1 M sodium chloride was used. The Amber ff99SB-ILDN (20) force-field was used to describe the receptors and the peptides. All simulations were carried out in the isothermal–isobaric (NPT) ensemble at 310 K and 1 atm. The velocity-rescaling thermostat (21) and the Parrinello-Rahman barostat (22, 23) were applied to keep the temperature and pressure constant. A time step of 2 fs was used for integrating the equations of motion. Nonbonded long-range electrostatic interactions were calculated using Particle Mesh Ewald (PME) (24). A 12 Å cut-off was used for van der Waals interactions, with long-range dispersion corrections for the energy and pressure (25). The neighbour list was updated every 20 steps. The solvated complexes systems were energy minimised, equilibrated (for 1.5 ns) and simulated using the protocol described in our previous work (16). Three unrestrained MD simulations, each 300ns long, were performed for each complex. All equilibrium MD simulations were performed using Gromacs 2019 (26) on the University of Bristol's High-Performance Clusters (BlueCrystal4 and BluePebble) and the Oracle Cloud Infrastructure (https://cloud.oracle.com/en_US/iaas). Accompanying preliminary simulations of the spike protein were run on ARCHER using time provided by EPSRC through HECBioSim under a COVID-19 call (https://www.hecbiosim.ac.uk). These were based directly on the previous work of Casalino *et al* (27).

Analysis

Analyses of the MD simulations were performed using Gromacs (26) and in-house tools. Images were produced with PyMOL (28, 29). The radius of gyration was used to determine the compactness of the S-peptide when bound to the different nAChRs (**Figure S10**). Principal component analysis (PCA) was used to examine the sampling of the peptide and to identify its relevant motions (**Figure S11**). All replicates for the three complexes were combined before the analysis, so that all share the same subspace, and their motions could be directly compared. 5400 frames (corresponding to one conformation per nanosecond per replicate per peptide) were used for the PCA. The first two principal components accounted for ~53% of the peptide dynamics and, hence, we restricted our analysis to PC1 and PC2 only.

PCA was also used to assess the sampling and equilibration/relaxation of the receptors, similarly to e.g. refs (30, 31). For this, all replicates for each complex were combined, and two conformations per nanosecond per replicate (totalling 1801 frames) were used for this analysis. PCA, together with the RMSD of the receptors over time, suggests that all the systems were equilibrated after 50 ns (**Figure S9**). The RMSD values for the ECDs of the human α4β2 and α7 nAChR are consistent with our previously published simulations (15).

The hydrogen bonds between the S-peptide and the nAChRs were monitored (**Figure S12**) using the hbond tool available in Gromacs (26). A hydrogen bond is considered present if the OH,NH-acceptor distance is smaller than 0.35 nm and the hydrogen-donor-acceptor is lower than 30°.

The time evolution of the distances between R682 of the S-peptide and the conserved aromatic residues lining the nAChR orthosteric binding pocket, namely TyrA (α4Y126, α7Y115 and αY117 in the principal subunit of the human α4β2, human α7 and muscle-like receptor from *Tetronarce californica*, respectively), TrpB (α4W182, α7W171 and αW173), TyrC1 (α4Y223, α7Y210 and αY214 in the principal subunit), TyrC2 (α4Y230, α7Y217 and αY222) and TrpD (β282, α7W77, δW78 and γW72) in the complementary subunits) were determined using the distance tool (26) in Gromacs (**Figures S13-S15**).

MM-PBSA calculations

A molecular mechanics Poisson–Boltzmann surface area (MM-PBSA) approach was used to calculate the binding free energy (ΔG_{bind}) for each complex. In this approach, the contribution of nonpolar, polar and entropic terms to the overall free energy of binding is estimated from a MD simulation of the solvated complex (32, 33). Snapshots were taken every two nanoseconds per replicate per complex (a total of 453 frames per complex). Binding free energies were computed using g_mmpbsa (34). This tool uses Gromacs (26) and APBS (35) to determine the binding energy and contribution of each residue. The solvent-accessible surface area (SASA) model was used to calculate the non-electrostatic contribution to the solvation free energy, whereas the electrostatic contribution was estimated by solving the Poisson−Boltzmann (PB) equation. For the APBS calculations, a grid spacing of 0.5 Å was used with a twofold expansion in each dimension. An ionic strength of 0.10 M was used with radii of 0.95 and 1.81 Å for sodium and chloride ions. The entropy change on binding is particularly challenging to compute for the binding of a long, flexible peptide (an in general is not feasible because of the extremely long simulations that would be required) and shows high standard error compared to the other energetic terms. The entropic contribution will disfavour binding in all three receptors and is likely to be similar in all three. The calculated values are therefore most usefully analysed in terms of relative binding affinity to the three receptors.

In silico alanine-scanning mutagenesis

In silico alanine-scanning mutagenesis involves the sequential mutation of the residues in the proteins to alanine to identify the key determinants for the thermodynamic stability of a given complex. In this approach, the binding free energies for the original and alanine mutant complexes are calculated (mutating all residues at the interface, singly, to alanine), and the difference between the two values

($\Delta\Delta G_{bind}$) is a way to evaluate the contribution of each residue for the interface. In this work, the $\Delta\Delta G_{bind}$ was computed using the command-line Python application BudeAlaScan (https://pragmaticproteindesign.bio.ed.ac.uk/balas/) (36, 37). This application uses ISAMBARD (38) for structure manipulation and a customized version of the Bristol University Docking Engine (BUDE) (39) for energy calculations. Snapshots were taken every three nanoseconds, a total of 303 frames per complex. The results were averaged over all frames (**Figures S20-S24**).

Characterization of the S-peptide in MD simulations of the full-length model of the glycosylated SARS-CoV-2 spike

To examine the conformational dynamics and the accessibility of S-peptide (Y674-R685 region) in the glycosylated SARS-CoV-2 spike, we analysed the extensive all-atom MD simulations conducted previously by some of us (27). In that work, two sets of simulations were performed on two full-length models of the glycosylated spike, a total of ~4.2 μs in the open (1 RBD 'up', 2 'down') and ~1.7 μs in the closed (all 3 RBDs 'down') states, which were based on 6VSB (40) and 6VXX (41) cryoEM structures, respectively. In these simulations, the models were cleaved at the S1/S2 site (i.e., between R685 and S686) to model the physiological state of the S-peptide. We remark that in 6VSB the Y674-R685 loop is entirely missing, whereas in 6VXX only three residues (674-676) were solved. Therefore the missing residues of this loop were *de-novo* modelled as described in Casalino *et al*. (27). Considering that the spike is a homotrimer, these simulations provide a comprehensive total of ~12.6 μs and ~5.1 μs of sampling for S-peptide in the open and closed states, respectively. To elucidate the availability of S-peptide in the glycosylated full-length spike for binding to nAChRs, we investigated the conformational behaviour of the S-peptide, and characterized its accessibility in the presence of the glycan shield.

Accessible Surface Area

During the simulations of the glycosylated spike protein in both the open and closed states, the S-peptide establishes intermittent interactions with nearby N-glycans, especially N-603, N-657, N-717, N-801 and N-1074. To characterize the extent of the glycan shield, we calculated the accessible surface area (ASA) of the S-peptide (with and without glycans) using 15 different probes increasing in radius size from 1.4 Å to 15 Å, as described by Casalino *et al*. (27) Using a range of values approximates different size molecules, ranging from small molecules at 2–5 Å to larger peptide- and antibody-sized molecules at 10–15 Å (27). The ASA of the S-peptide was calculated across the replicate spike simulations at 2 ns intervals (**Figure S5**). The difference between the overall accessibility of the 'naked' protein (without glycans) and the glycan shielded area corresponds to the effective accessibility of the S-peptide in the presence of glycans. The ASA of the peptide in the presence of glycans is shown (as a function of probed radius) as the cyan-coloured area in **Figure S5**). Clearly, the peptide is accessible to solvent

(and therefore accessible for binding) in the fully glycosylated spike. The ASA varies between simulations, and between the three sites in the spike. There are indications of potentially differences in ASA of the peptide between the open and closed states of the spike. Indeed, the peptide shows a different amount of glycan shielding, with an average maximum shielding (across replicas and chains) of 47% in the open spike and 30% in the closed spike, at 15 Å probe radii (where the % indicates the degree of shielding, with 100% being completely shielded for the entire trajectory, and 0% being completely exposed) (**Figure S5**). In the open conformation (one RBD, in chain A, in the up conformation) the packing of the three monomers is somewhat different from the closed conformation. This causes differences in accessibility and glycan shielding between the two systems and between chains (**Figure S5**). Although the calculated ASA and glycan shielding values vary due to the high flexibility of the peptide and the glycans, this analysis shows that the S-peptide is weakly shielded, especially when the spike is in the closed state, and therefore is available for engaging with nAChRs. We also note that the same region of the spike has been shown by experiments to bind to human neuropilin-1 receptors (42), which is clear evidence of its accessibility and ability to bind, and of the feasibility of interaction of the spike with a membrane-bound host receptor *in vivo*.

Radius of gyration

The radius of gyration (*Rg*) of the S-peptide in the spike protein was calculated from MD simulations of the glycosylated full-length spike (**Figure S6**). Notably, the closed system exhibits a single *Rg* population, with an average of 0.78 +/– 0.09 nm, while the open system shows a wider distribution, with an average *Rg* value of 0.75 +/– 0.13 nm. The range of *Rg* values is comparable to that observed in the peptide-only simulations (**Figure S10**) These results show that the S-peptide adopts an extended, solvent-accessible conformation in the spike (**Figure S6B**). These results also provide evidence of different behaviour of the S-peptide between the open and closed spikes, possibly resulting from a slightly altered packaging of the three monomers. Some indications of differences between open and closed spike states is also apparent from the ASA analysis. This suggests that the closed and open states may have different binding propensities at this site.

Supporting figures

```
SARS-CoV-2 S       674 - YQTQTNSPRRAR - 685
α-bungarotoxin      50 - CDAFCSS-RGKV -  60
RABV G             208 - CDIFTNS-RGKR - 218
```

Figure S1. Sequence alignment of the Y674-R685 region in the spike protein from SARS-CoV-2 and two known nAChR antagonists, namely α-bungarotoxin from *Bungarus multicinctus* (4-6) and glycoprotein (G) from *Rabies lyssavirus* (formerly *Rabies virus*) (43-45). The sequence alignments shown here were taken from the work of Changeux *et al.* (8). The residue numbers refer to the following UniProt codes: P0DTC2 (spike protein), P60615 (α-bungarotoxin) and P15199 (G protein).

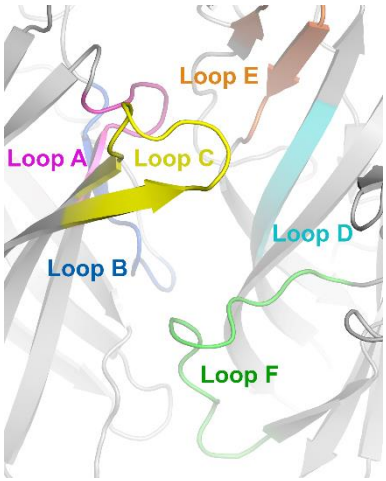

Figure S2. Detailed view of the nAChR binding pocket. This image is of the cryoEM structure of the muscle-type receptor from *Tetronarce californica* (PDB code: 6UWZ) (1). The structural motifs lining the pocket are highlighted with the following colour scheme: loop A, magenta; loop B, blue; loop C, yellow; loop D, cyan; loop E, orange; loop E, green.

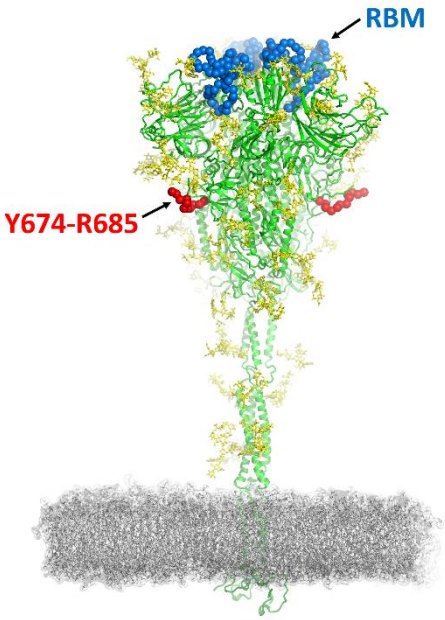

Figure S3. Overview of the three-dimensional structure of the spike protein from SARS-CoV-2. The model shown here represents the complete, fully glycosylated, SARS-CoV-2 spike protein in the closed state after furin cleavage. This model was taken from Casalino *et al*. (27). The spike protein is coloured in green, with glycans depicted in yellow. The Y674-R685 region (proposed to interact with nAChRs) is shown with red spheres. The receptor-binding motif (S438-Q506 region) which is known to bind to ACE2 (40, 46) is highlighted in blue.

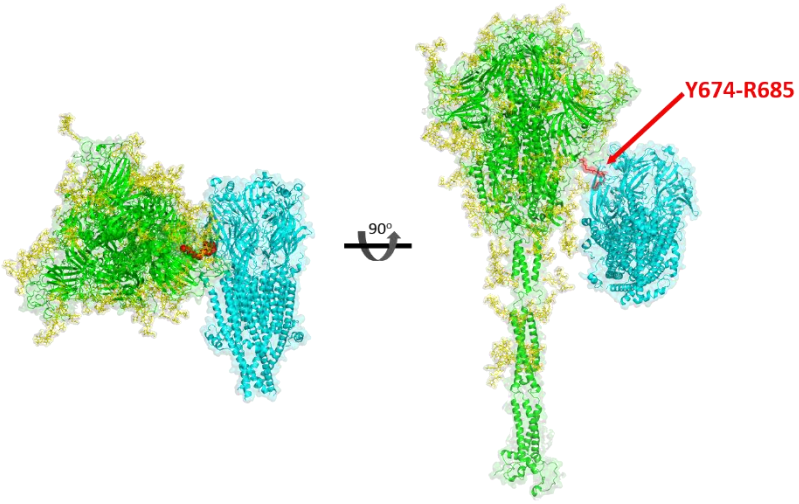

Figure S4. A model for the interaction between the SARS-CoV-2 spike protein and nAChR. Modelling suggests that interaction of the spike and nAChRs is possible with the two proteins oriented in a non-parallel arrangement to one another. In this figure, the model for the full-length closed glycosylated

spike (after furin cleavage) was developed by Amaro and co-workers (27). For the nAChR, the cryoEM structure of the muscle-type receptor from *Tetronarce californica* (1) was used. The spike protein is coloured in green (with the glycans in yellow) and the nAChR is highlighted in cyan. The Y674-R685 region in the spike is shown with red spheres. It should be noted that both proteins are membrane bound (expected to be bound in the viral envelope, and the host cell membrane, respectively). This interaction may therefore require deformation of one or both membranes, and/or bending of the spike. Experiments and (coarse-grained) models show that the spike is capable of significant bending (47-50). We also note that the human neuropilin-1 receptor has been shown to interact with the spike protein (42), via a region of the spike analogous to the one predicted to interact with nAChRs here.

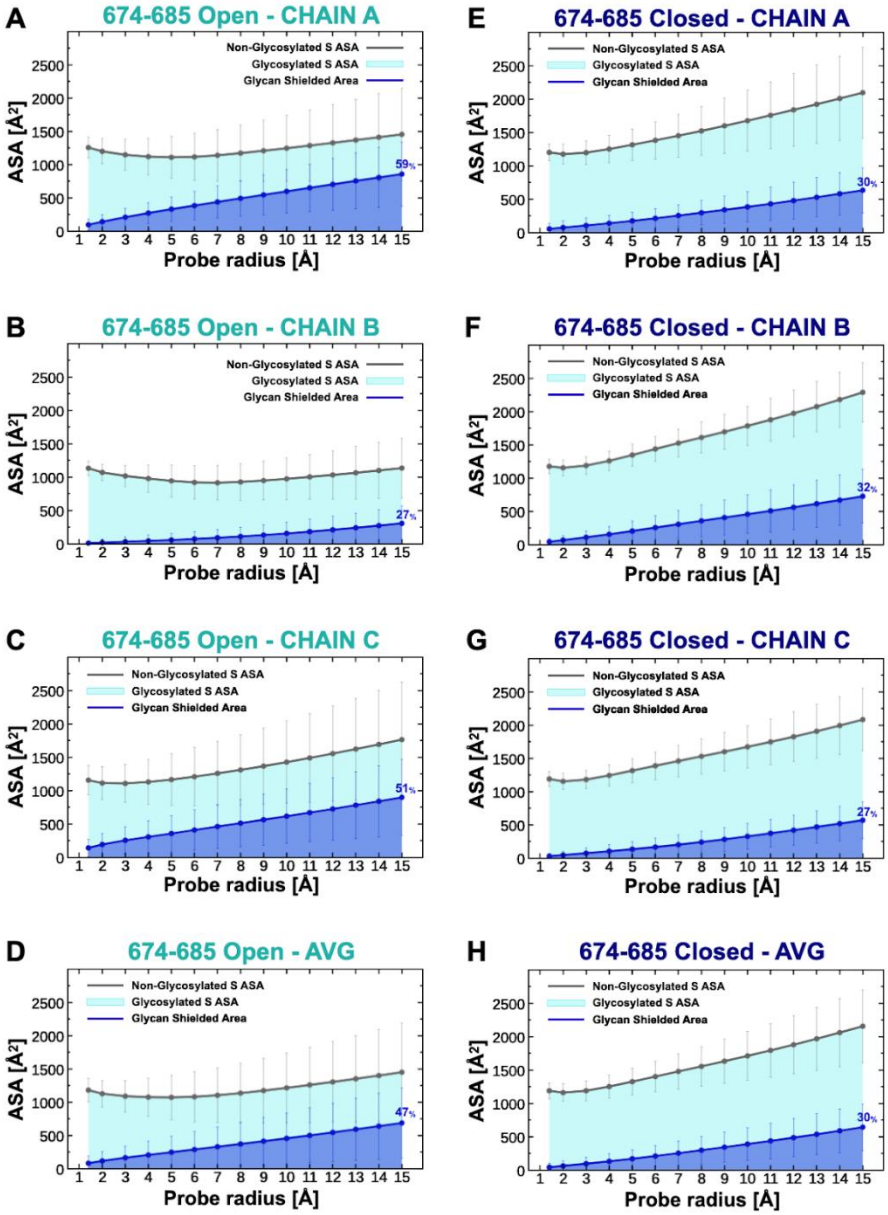

Figure S5. Accessible surface area (ASA) of the Y674-R685 region in the context of the fully-glycosylated full-length SARS-CoV-2 spike from Casalino *et al.* (27). The ASA of residues 674-685

(corresponding to the S-peptide), and the area shielded by glycans, at multiple probe radii from 1.4 Å (water molecule) to 15 Å are calculated from the all-atom MD simulations of the full-length models of the glycosylated SARS-CoV-2 spike protein (27) in the open (**A-D**) and closed states (**E-H**). The area of 674-685 shielded by the glycans is presented in blue (rounded % values are reported), whereas the grey line represents the accessible area of 674-685 in the absence of glycans. Highlighted in cyan is the area of 674-685 that remains accessible in the presence of glycans. Per-chain analysis of 674-685 in the open (one RBD up) state is reported in panels **A**, **B** and **C**, showing the values for the 674-685 in chain A (RBD-up), B and C, respectively. Similarly, panels **E, F** and **G** display the per-chain analysis of 674-685 in the closed spike, where chains A, B and C are all in the 'down' conformation. The calculated values have been averaged across replicas and the error bars correspond to +/- standard deviation. Panels **D** (open) and **H** (closed), the ASA and glycans shield values show averages also across chains. Note that panels **D** and **H** in this image show the same information as panels **B** and **C** in **Figure 4**.

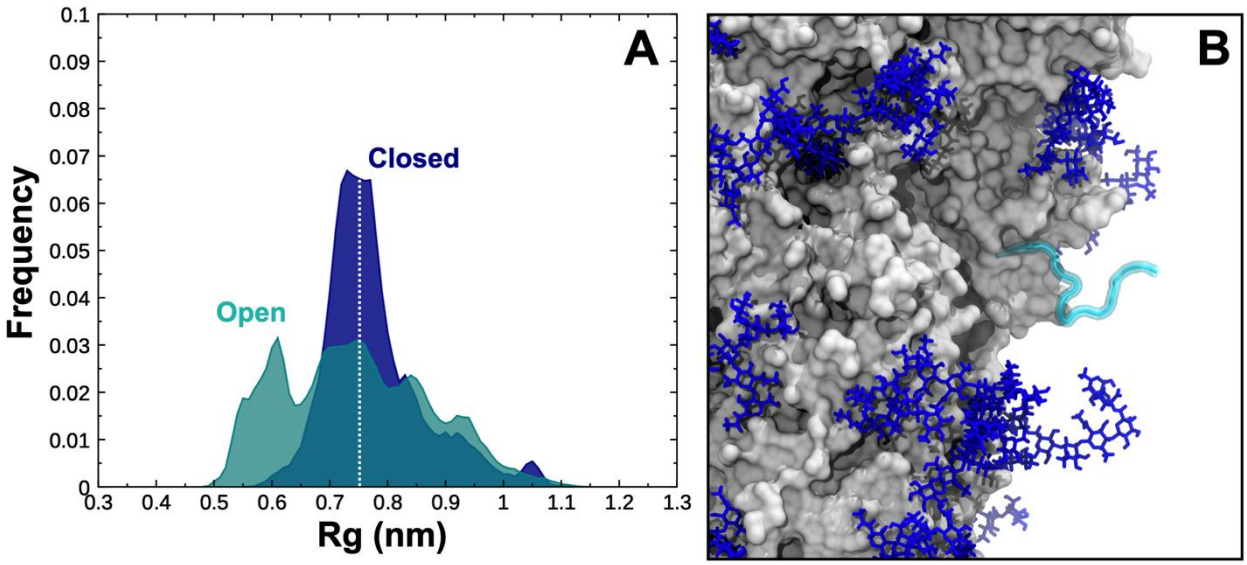

Figure S6. (A) Radius of gyration (*Rg*, nm) distribution for the S-peptide from simulations of the full-length model of the cleaved, glycosylated spike in the open (teal) and closed states (blue). The two distributions are shown as (smoothed) normalized frequency histogram (bin width of 0.01 nm), where all the relative bin frequencies (i.e., number of frames) are normalized to sum to one. Normalization was done using the respective total number of frames for each system. (**B**) A snapshot taken from the simulations of the spike in the closed state showing one of the three S-peptides protruding into the solvent, with a *Rg* of 0.75 nm. The protein is depicted with a grey surface, whereas the S-peptide is shown as a cyan ribbon. The glycans are illustrated with blue sticks.

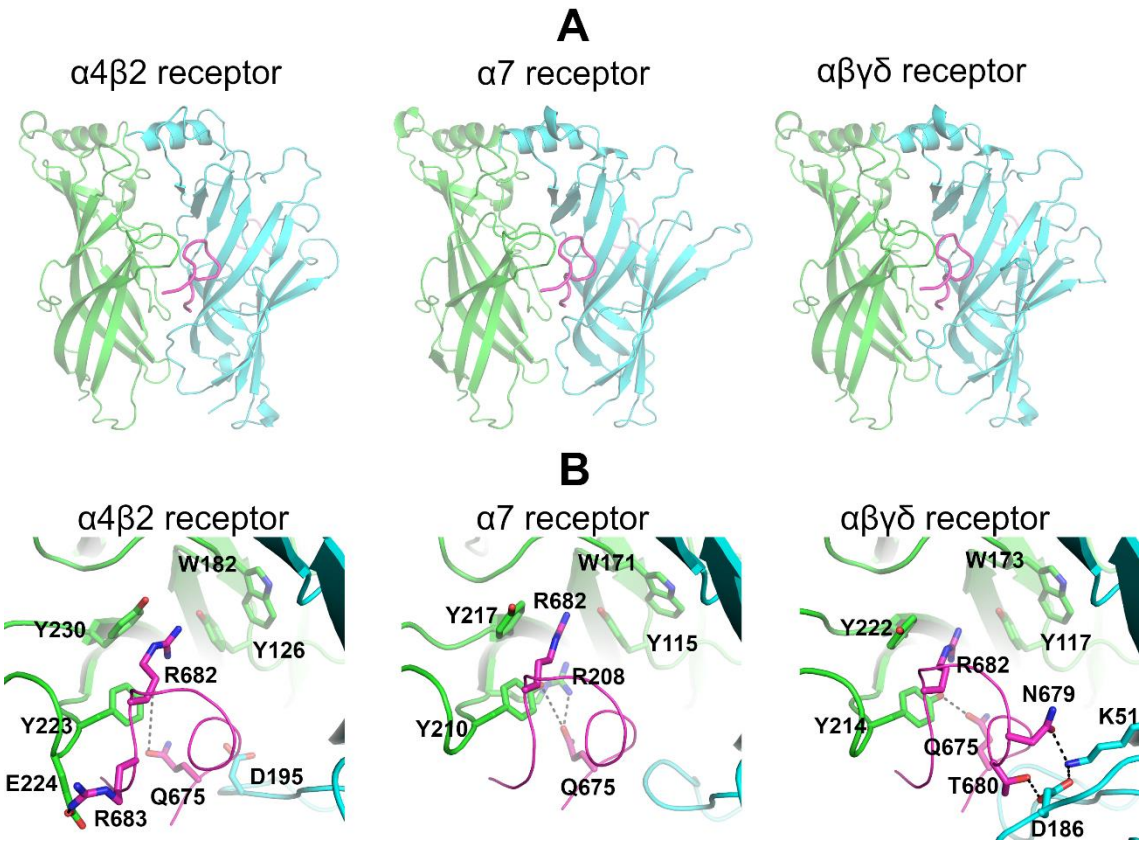

Figure S7. Binding of SARS-CoV-2 S-peptide to the second binding pocket in different nAChRs in the beginning of the simulations. **(A)** Overall view of the peptide-receptor complexes. The S-peptide (region Y674-R685) is highlighted in magenta, whereas the principal and complementary subunits are coloured in green and cyan, respectively. All three models show the peptide conformation when bound to the second pocket. **(B)** Closeup view of the peptide-receptor interaction region in each nAChR. Residues that interact directly with the peptide are shown with sticks.

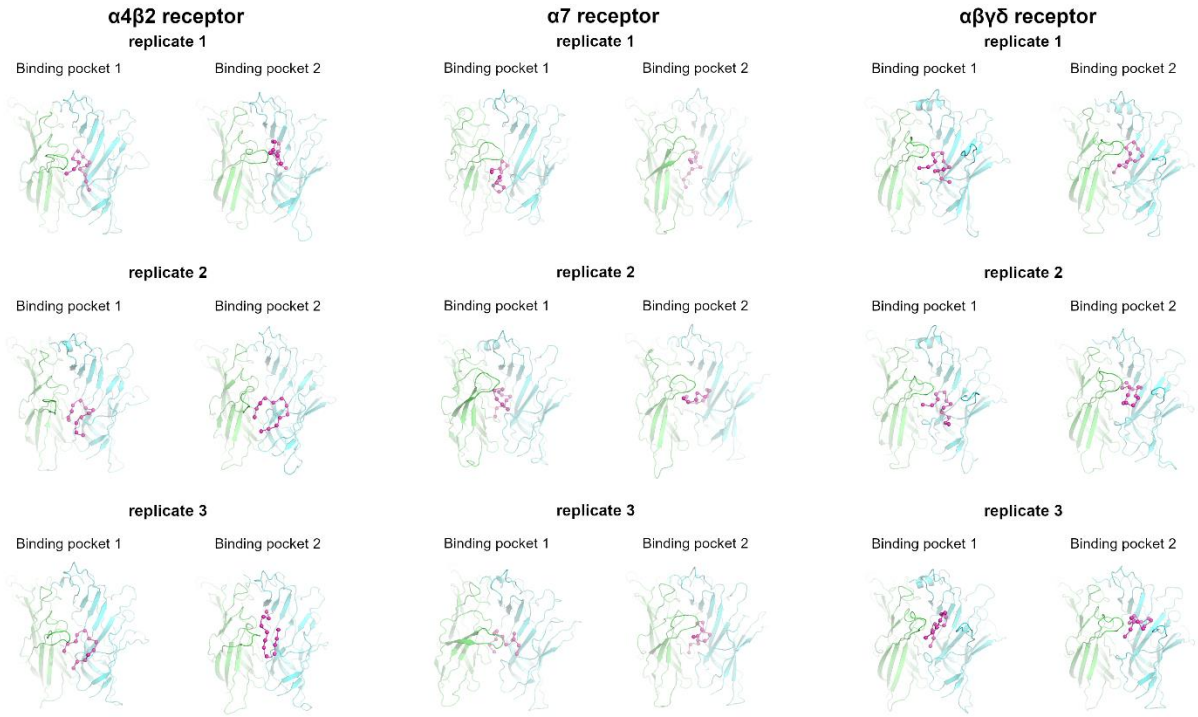

Figure S8. Binding mode of the S-peptide in the human α4β2, human α7 and muscle-like αβγδ receptor from *Tetronarce californica* after 300 ns of simulation, from three replicates in each case. The peptide is shown in magenta, and the principal and complementary subunits are coloured in green and cyan, respectively. Please zoom into the image for detailed visualisation.

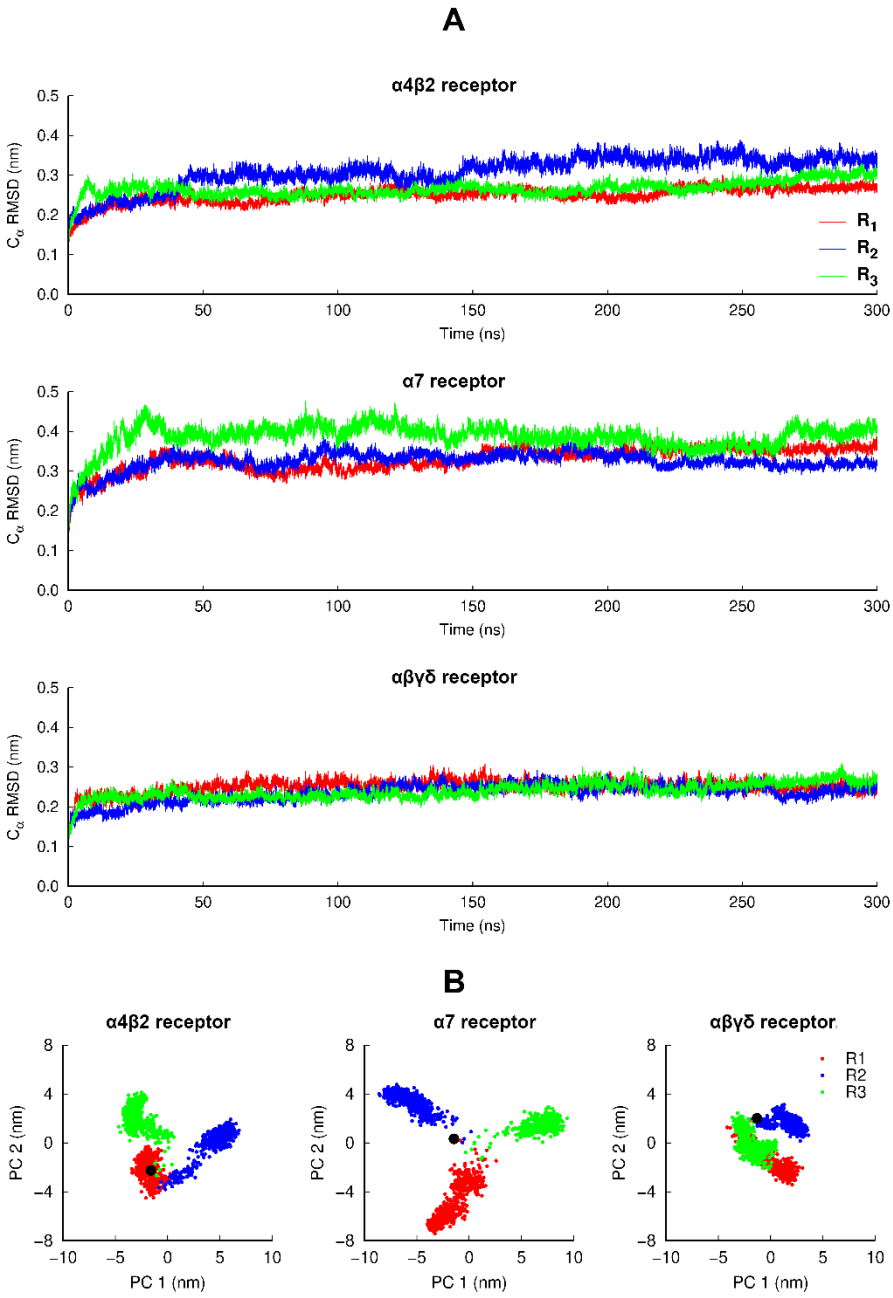

Figure S9. **(A)** Time evolution of the C_α RMSD of the individual replicates for the human α4β2, human α7 and muscle-like αβγδ receptor from *Tetronarce californica*. The C_α RMSD was calculated relative to the starting structures. **(B)** PCA of all replicates for the α4β2, α7 and αβγδ receptors. All three replicates for each system were combined before the analysis, and each trajectory contained two conformations per nanosecond per replicate (totalling 1801 frames) with all the C_α atoms of the protein. The black dot corresponds to the structure used as the starting point for the replicates. Note that the different replicates sample different regions of conformational space, thus improving the overall sampling for each system.

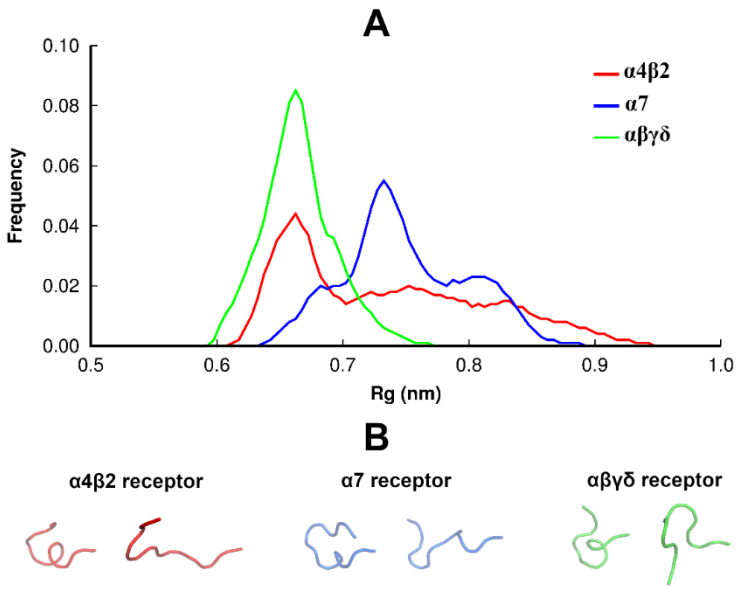

Figure S10. (**A)** Radius of gyration (*Rg*) distribution for the S-peptide when bound to human α4β2 (red line), human α7 (blue line) and muscle-like αβγδ receptor from *Tetronarce californica* (green line) nAChRs. The histograms reflect the *Rg* of peptides bound at both sites from the 3 independent simulations performed for each complex. (**B)** The most compact and extended conformations adopted by the S-peptide when bound to the different receptors.

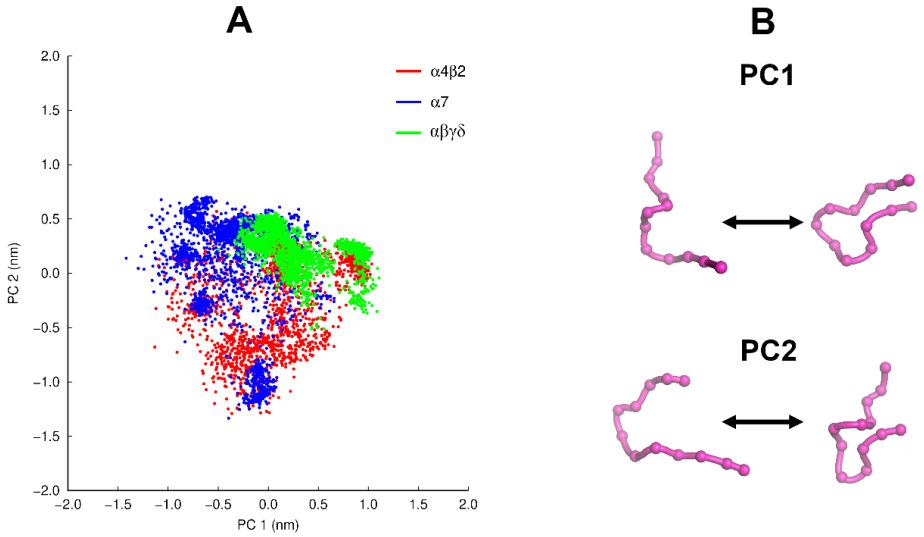

Figure S11. (**A)** PCA for the S-peptide in the different nAChRs. (**B)** Conformations indicating motions associated with PC1 and PC2. Each trajectory contained two conformations per nanosecond per replicate per peptide (totalling 5400 frames) with all the C_α atoms of the peptide used for PCA. PC1 and PC2 correspond to 29% and 24% of the data, respectively. Please zoom into the image for detailed visualization.

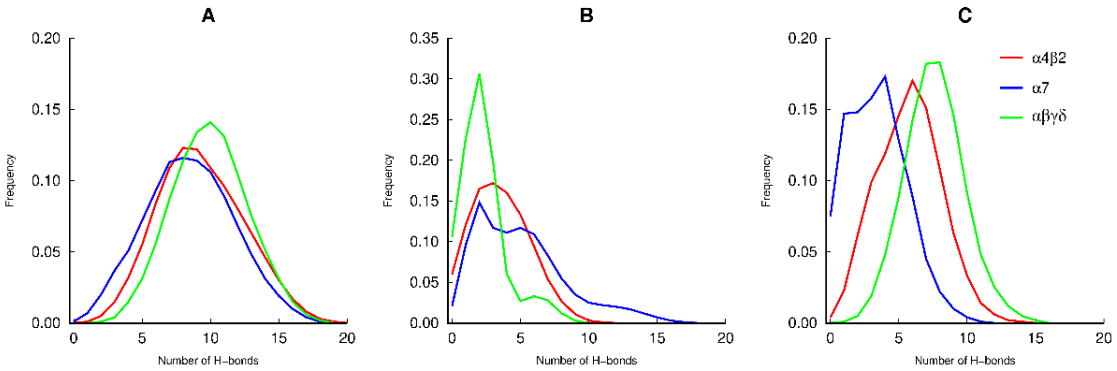

Figure S12. Numbers of hydrogen bonds observed between the S-peptide and each receptor in simulations of nAChR/S-peptide complexes. (**A)** Overall number of hydrogen bonds. (**B** and **C)** Number of hydrogen bonds with the principal (**B**) and complementary (**C**) subunits. Please zoom into the image for detailed visualization.

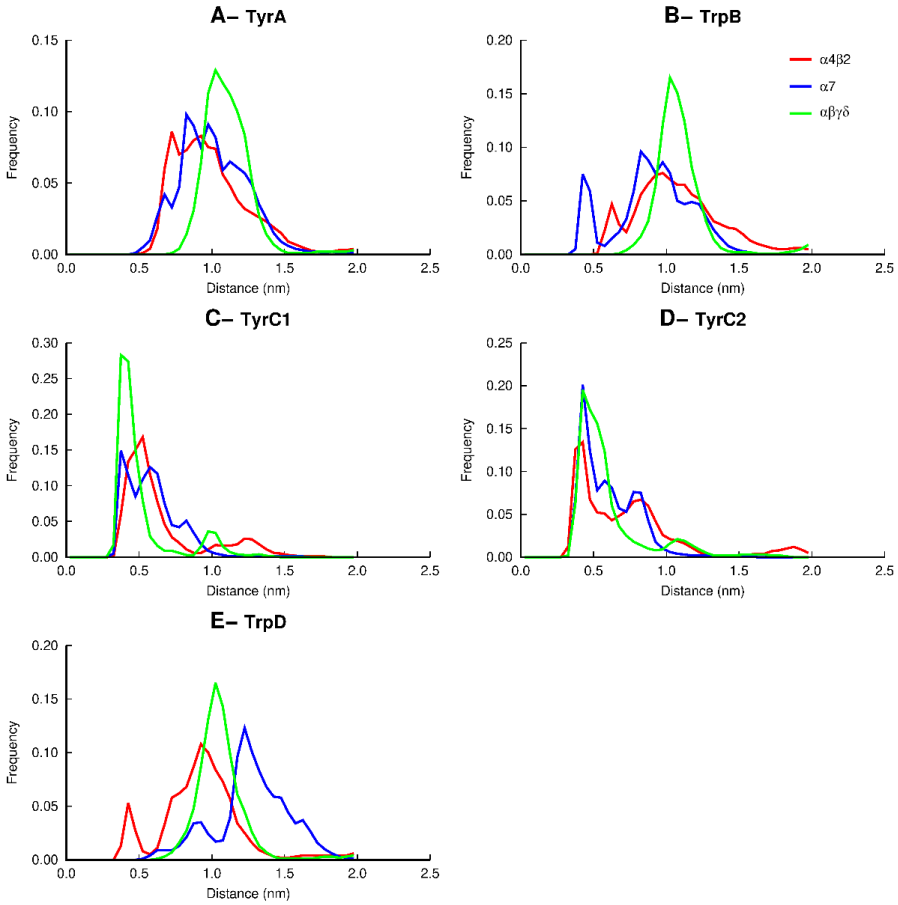

Figure S13. Distributions of the distances between R682 of the S-peptide and conserved aromatic residues lining the nAChR binding pocket from simulations of the S-peptide/nAChR complexes. Red denotes results for α4β2; blue denotes α7; and green denotes muscle-like receptor from *Tetronarce californica.* Distribution of the distance between the sidechain of R682 of the S-peptide and: **(A)** TyrA

(α4Y126, α7Y115 and αY117 in the principal subunit of the human α4β2, human α7 and muscle-like receptor from *Tetronarce californica*, respectively); **(B)** TrpB (α4W182, α7W171 and αW173); **(C)** TyrC1 (α4Y223, α7Y210 and αY214 in the principal subunit); **(D)** TyrC2 (α4Y230, α7Y217 and αY222); and **(E)** TrpD (β282, α7W77, δW78 and γW72) in the complementary subunits). Note that the sequence numbering used here refers to the following sequences: human α7 (UniProt code P36544), human α4 (UniProt code P43681); human β2 (UniProt code P17787); *Tetronarce californica* α (UniProt code P02710); *Tetronarce californica* δ (UniProt code P02718); *Tetronarce californica* γ (UniProt code P02714); and SARS-CoV-2 spike protein (Uniprot code P0DTC2). The histograms include data for the distances for both binding pockets in each simulation. Please zoom into the image for detailed visualization.

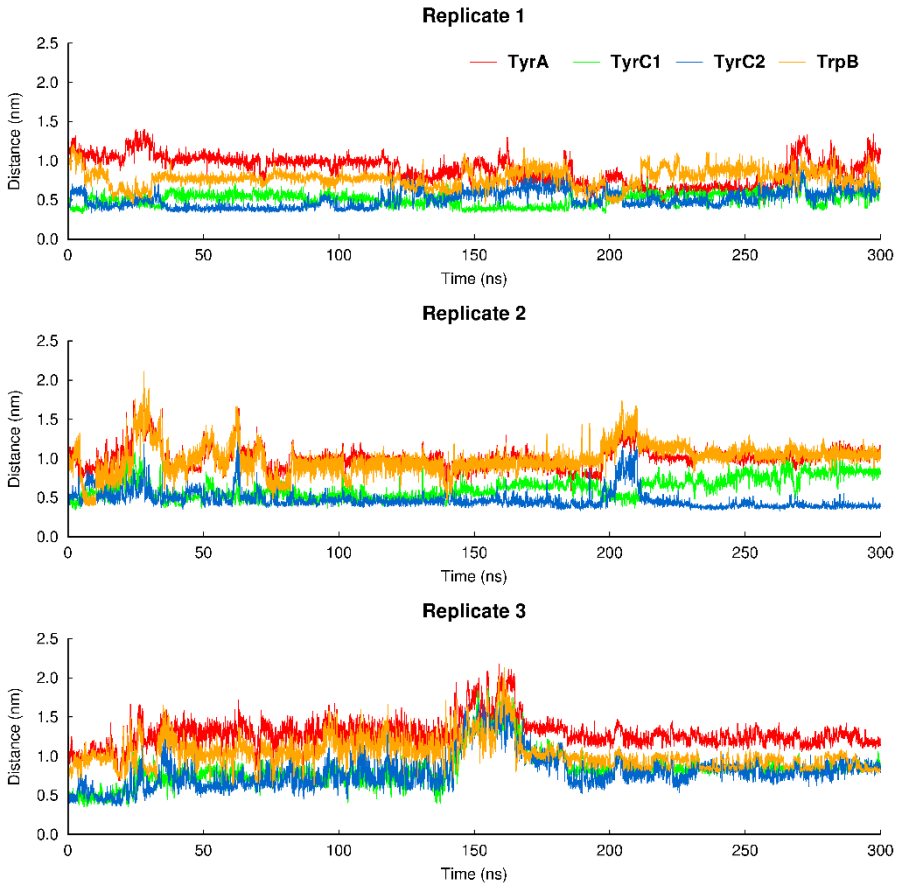

Figure S14. Time evolution of the distances between the sidechains of R682 of the S-peptide and TyrA, TrpB, TyrC1 and TyrC2 in the first binding pocket of the α7 nAChR.

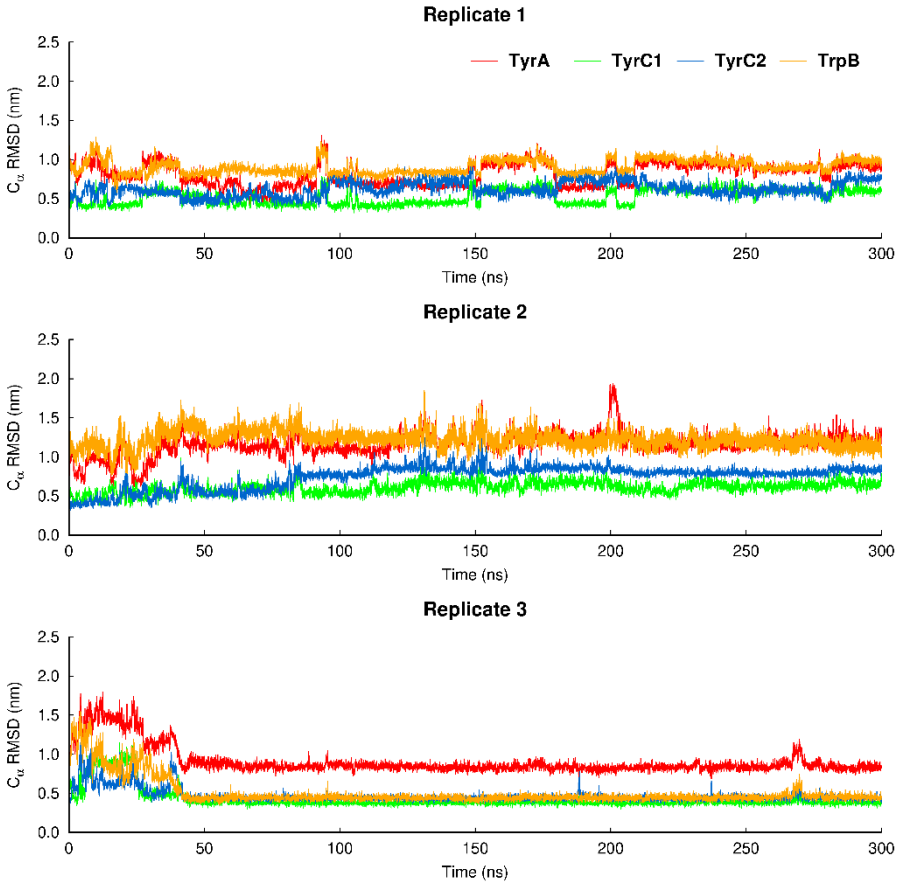

Figure S15. Time evolution of the distances between the sidechains of R682 on the S-peptide and TyrA, TrpB, TyrC1 and TyrC2 in the second binding pocket of the α7 nAChR.

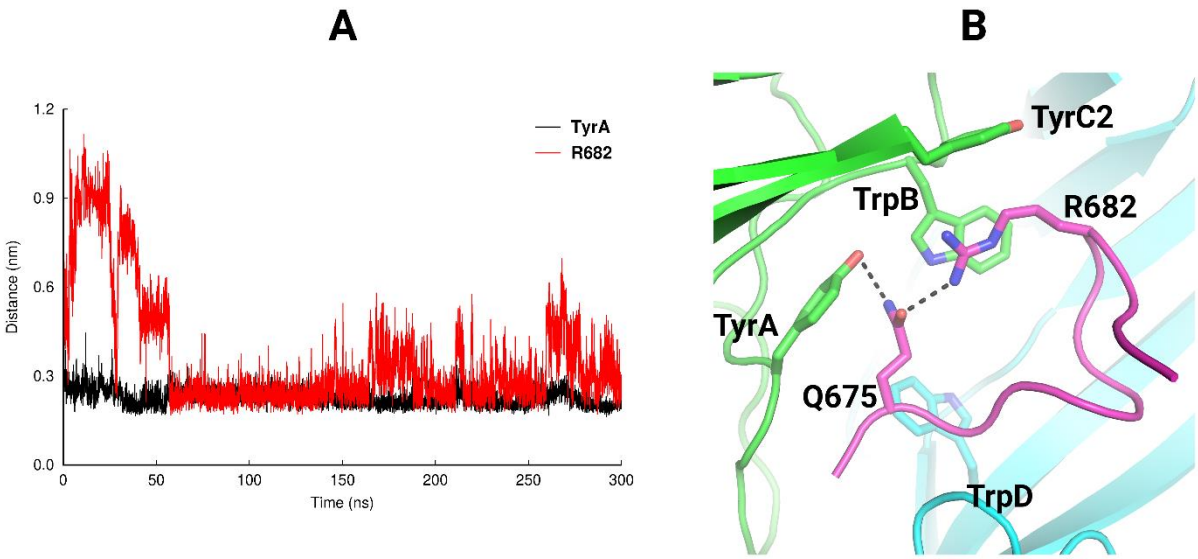

Figure S16. Hydrogen bond network involving TyrA in the α7 complex, in which a direct interaction between TrpB and R682 is present. **(A)** Time evolution of the minimum distance between Q675 and

R682 and Q675 and TyrA in replicate 3. (**B)** Closeup view of the hydrogen bond network involving TyrA, Q675 and R682 in a representative conformation of the α7 complex, in which direct interaction between TrpB and R682 is observed**.** Note that this image shows the same conformation as **Figure 3** but in a different orientation. The principal and complementary subunits of the human α7 receptor are coloured in green and cyan, respectively. The S-peptide is highlighted in magenta. Hydrogen bonds involving Q675 are highlighted with dashed lines. Part of the loop C region from the receptor is not shown, for clarity.

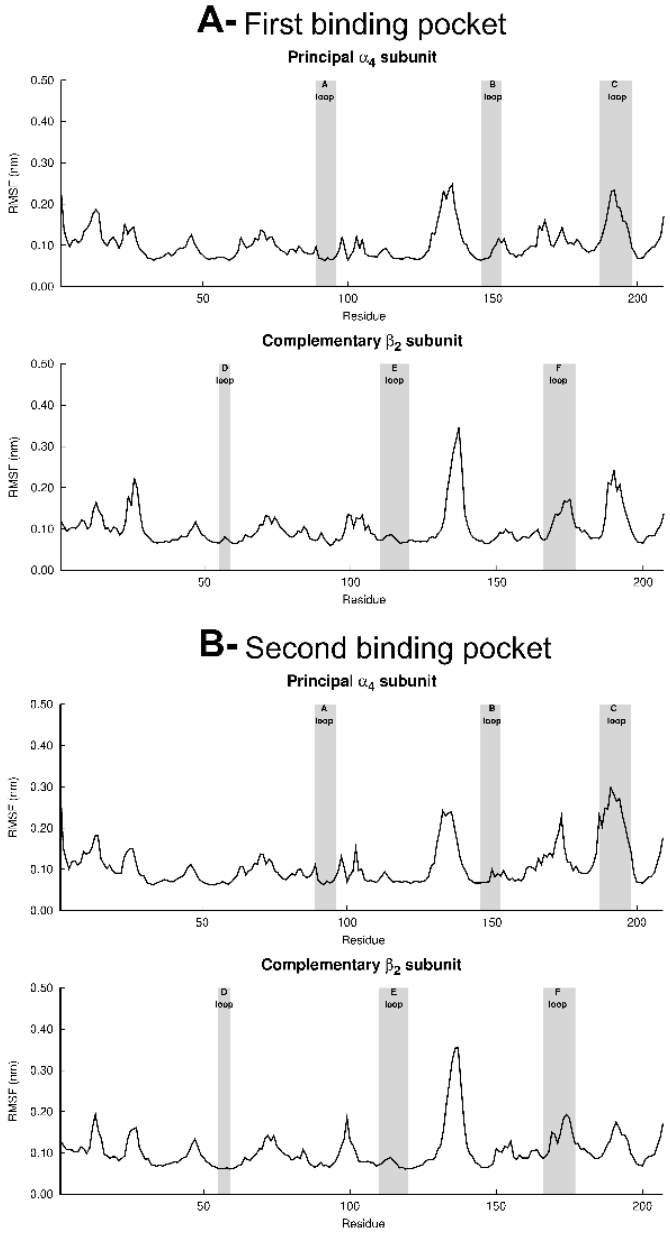

Figure S17. Average RMSF (averaged over the individual RMSFs for the three replicate MD simulations) for the first (**A**) and second (**B**) binding pockets in the α4β2 complex. Please zoom into the image for detailed visualisation.

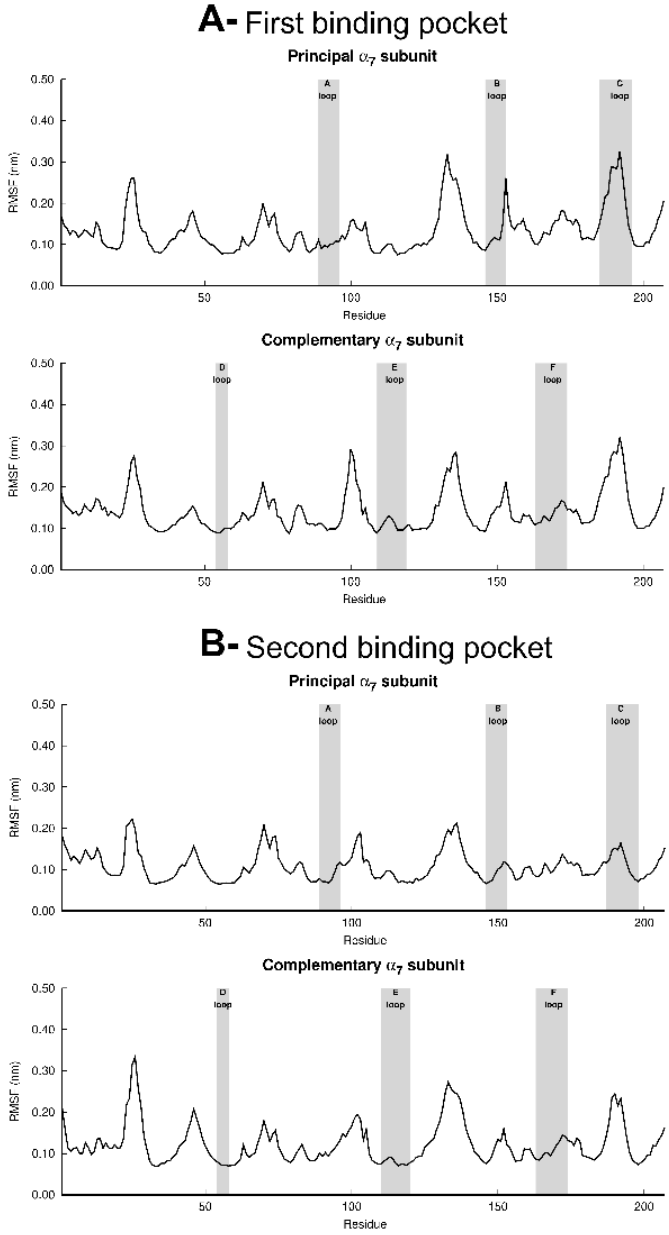

Figure S18. Average RMSF (averaged over the individual RMSFs for the three replicate MD simulations) for the first (**A**) and second (**B**) binding pockets in the α7 complex. Please zoom into the image for detailed visualisation.

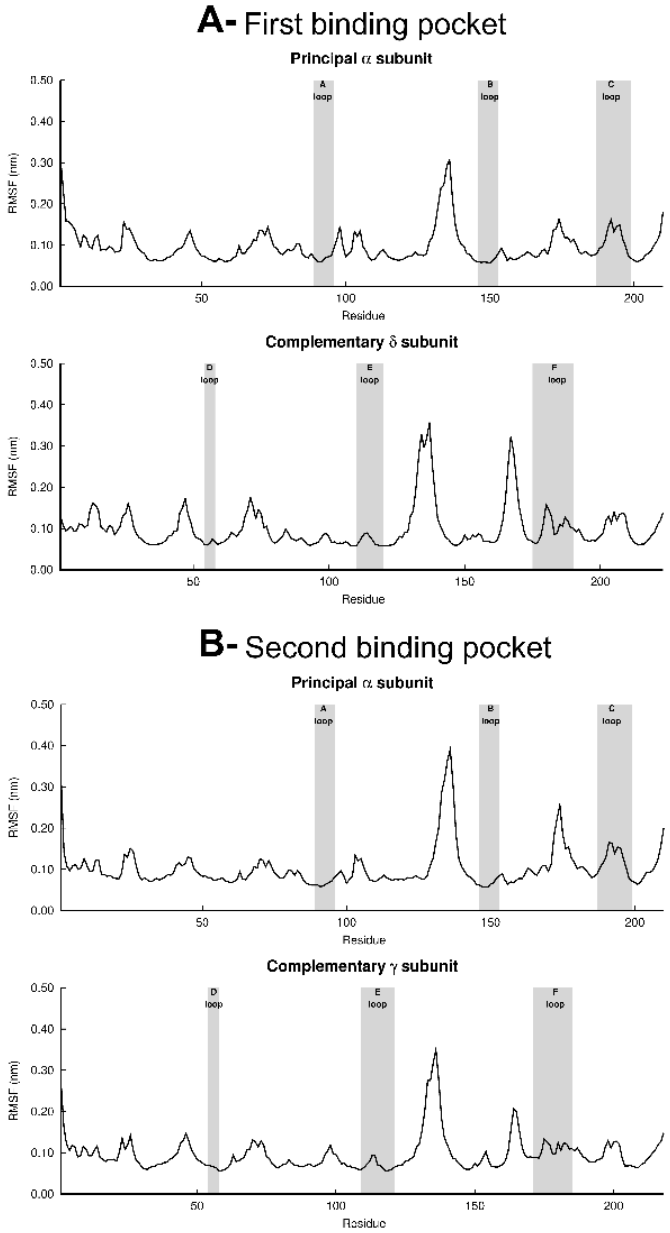

Figure S19. Average RMSF (averaged over the individual RMSFs for the three replicate MD simulations) for the first (**A**) and second (**B**) binding pockets in the muscle-like αβγδ complex. Please zoom into the image for detailed visualisation.

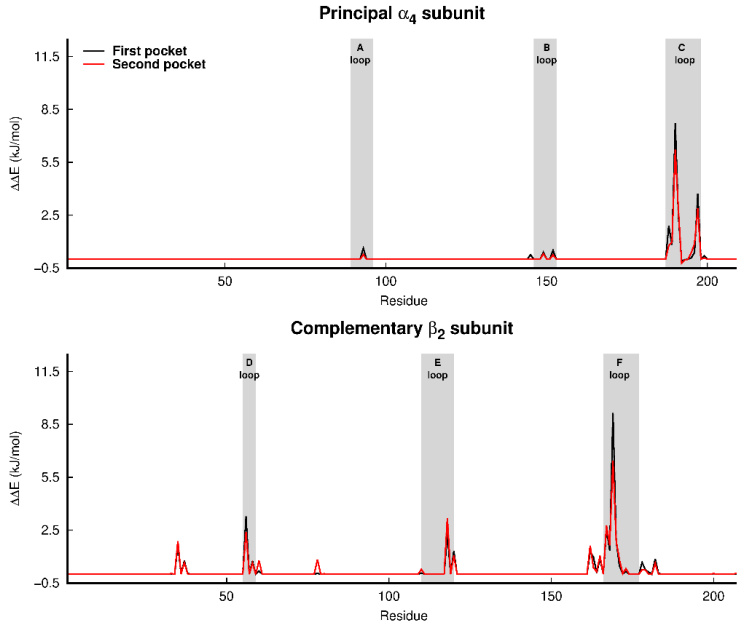

Figure S20. Average calculated $\Delta\Delta G_{bind}$ from the BUDE alanine-scanning mutagenesis (https://pragmaticproteindesign.bio.ed.ac.uk/balas/) (36, 37) for the human α4β2 nAChR (for details see the '*In silico* alanine-scanning mutagenesis' section above). The average was determined over the three replicates. Note that the $\Delta\Delta G_{bind}$ corresponds to the difference between alanine mutant and wild-type complexes, and a positive $\Delta\Delta G_{bind}$ value means that the mutation to alanine destabilizes the complex. Please zoom into the image for detailed visualization.

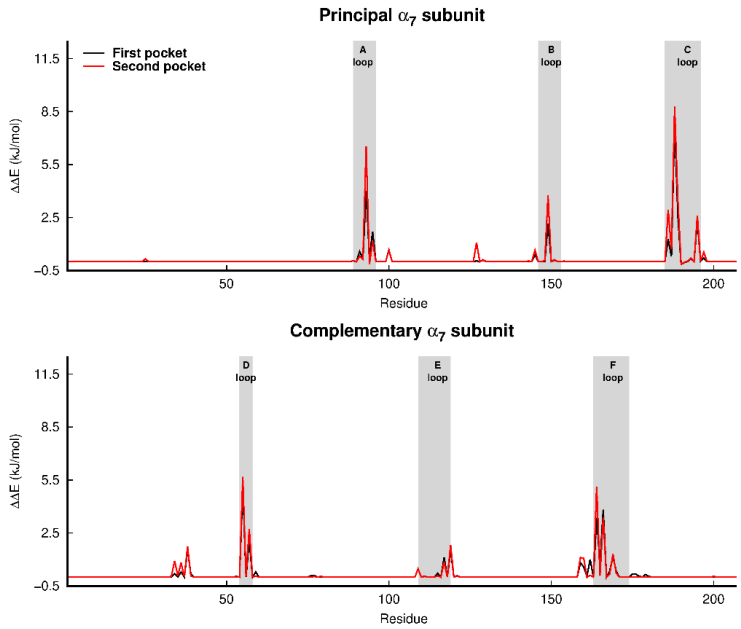

Figure S21. Average predicted $\Delta\Delta G_{bind}$ from the BUDE alanine-scanning mutagenesis (https://pragmaticproteindesign.bio.ed.ac.uk/balas/) (36, 37) for the human α7 nAChR. For more details, see the legend of **Figure S20**. Please zoom into the image for detailed visualization.

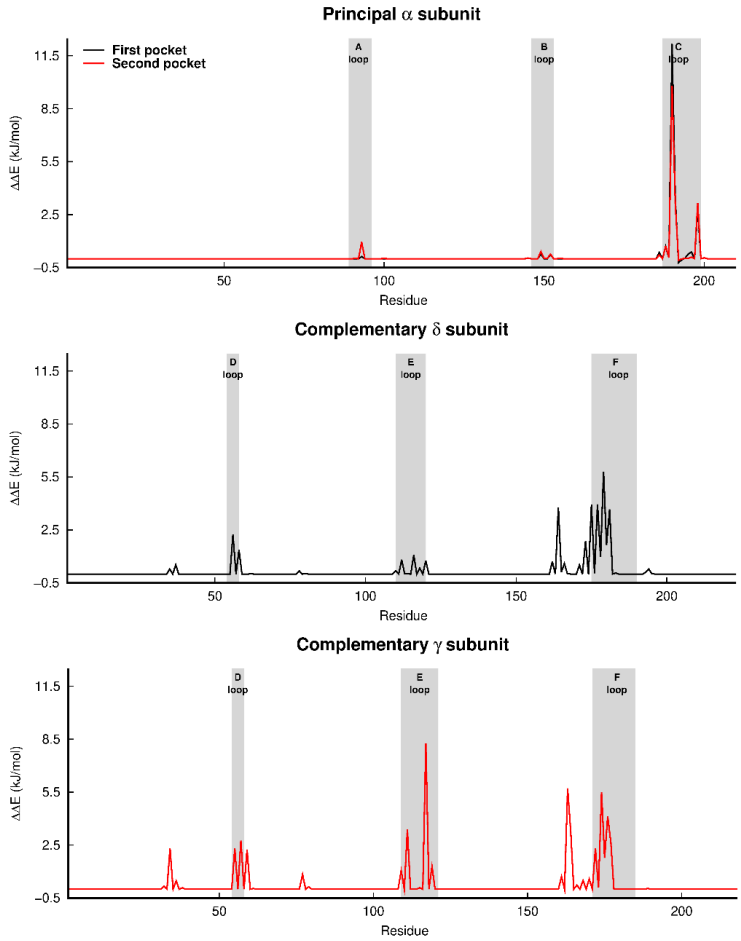

Figure S22. Average predicted $\Delta\Delta G_{bind}$ from the alanine-scanning mutagenesis using BUDE Alanine Scan (https://pragmaticproteindesign.bio.ed.ac.uk/balas/) (36, 37) for the muscle-like αβγδ nAChR from *Tetronarce californica*. For more details, see the legend of **Figure S20**. Please zoom into the image for detailed visualization.

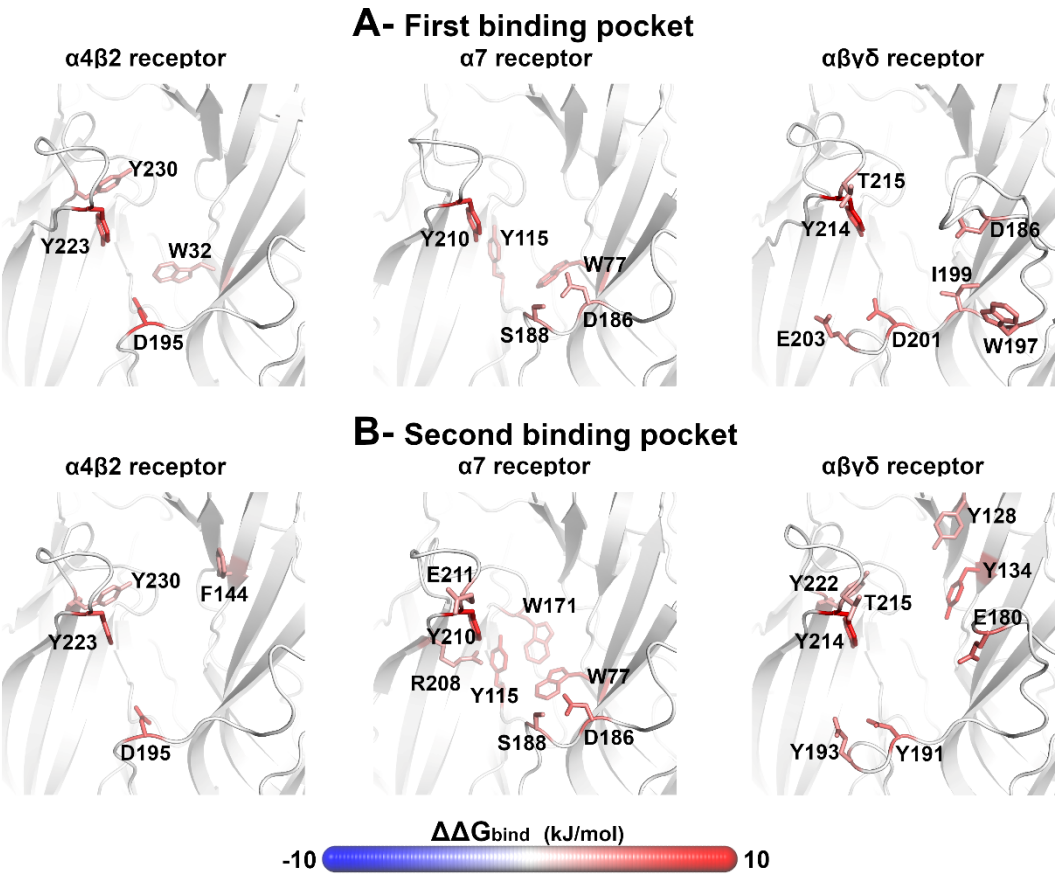

Figure S23. Hot spots in the binding interface of the receptors that favour binding, identified from BUDE Alanine Scanning. Note that the $\Delta\Delta G_{bind}$ corresponds to the difference between the alanine mutant and wild-type complexes. In this image, the red colour indicates a stabilizing contribution to the complex whereas blue indicates a destabilizing contribution.

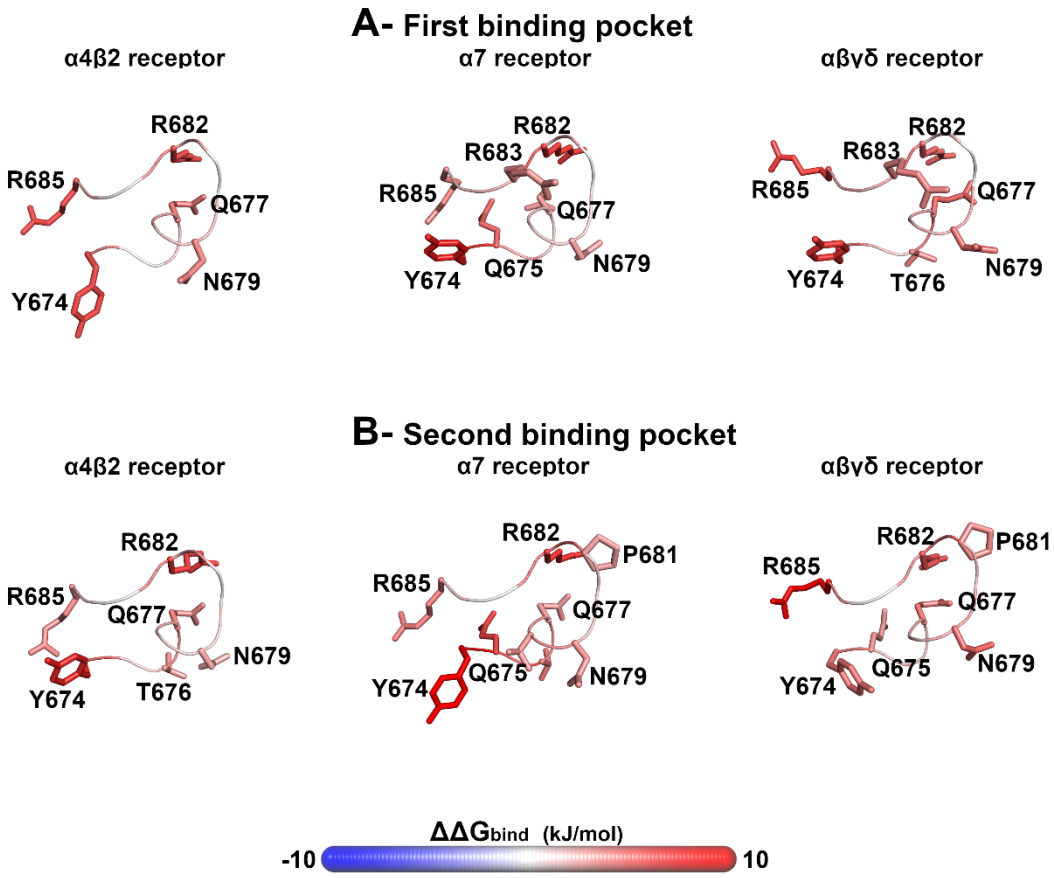

Figure S24. Hotspots in the S-peptide from BUDE Alanine Scanning. The $\Delta\Delta G_{bind}$ corresponds to the difference between the alanine mutant and wild-type complexes. In this image, the red colour indicates a stabilizing contribution to the complex whereas blue indicates a destabilizing contribution.

Supporting Tables

Table S1: MM-PBSA relative binding energy values for the S-peptide in the human α4β2, human α7 and muscle-like αβγδ nAChR from *Tetronarce californica*. Numbers in brackets represent the standard deviations. Note that the values reported in this table do not contain the entropic contribution to the binding energy.

	ΔG_{bind} for the α4β2 complex (kJ/mol)		
	Replicate 1	**Replicate 2**	**Replicate 3**
First pocket	–308.8 (59.6)	–171.1 (51.6)	–167.9 (97.2)
Second pocket	–274.2 (97.3)	–163.5 (92.0)	–209.5 (86.1)
	ΔG_{bind} for the α7 complex (kJ/mol)		
	Replicate 1	**Replicate 2**	**Replicate 3**

First pocket	–157.0 (78.9)	–193.2 (51.0)	–203.3 (48.0)
Second pocket	–62.9 (72.7)	–152.8 (93.7)	–129.2 (100.6)
	ΔG_{bind} for the muscle-like αβγδ complex (kJ/mol)		
	Replicate 1	**Replicate 2**	**Replicate 3**
First pocket	–441.0 (50.2)	–420.8 (45.7)	–261.2 (73.7)
Second pocket	–313.2 (61.0)	–464.5 (66.1)	–396.8 (81.7)

Table S2: BUDE Alanine-scanning predicted average $\Delta\Delta G_{bind}$ values for the hot-spots (–3 kJ/mol ≥ residue contribution ≤ 3 kJ/mol) in the second binding pocket of the receptors. The average was calculated over the three replicates. Numbers in brackets represent the standard deviations (calculated over 303 MD frames per complex). The $\Delta\Delta G_{bind}$ corresponds to the difference between the alanine mutant and wild-type complexes, and a positive $\Delta\Delta G_{bind}$ value means that the mutation to alanine destabilizes the complex.

Second binding pocket					
α4β2 receptor		**α7 receptor**		**Muscle-like αβγδ receptor**	
residue	$\Delta\Delta G_{bind}$ (kJ/mol)	residue	$\Delta\Delta G_{bind}$ (kJ/mol)	Residue	$\Delta\Delta G_{bind}$ (kJ/mol)
β2D195	6.2 (2.9)	α7Y210	8.9 (1.9)	αY214	9.8 (2.1)
α4Y223	6.2 (2.3)	α7Y115	6.7 (2.4)	γY134	8.1 (1.7)
α4Y230	3.3 (2.6)	α7W77	5.6 (2.2)	γD191	5.7 (2.2)
β2F144	3.2 (1.6)	α7D186	5.3 (2.4)	γE180	5.5 (3.3)
		α7W171	3.9 (1.9)	γE193	4.0 (2.4)
		α7S188	3.5 (1.7)	γY128	3.4 (2.5)
		α7E211	3.3 (1.4)	αY222	3.2 (1.4)
		α7R208	3.0 (1.9)	αT215	3.0 (2.0)

References

1. Rahman, M. M., J. Teng, B. T. Worrell, C. M. Noviello, M. Lee, A. Karlin, M. H. B. Stowell, and R. E. Hibbs. 2020. Structure of the native muscle-type nicotinic receptor and inhibition by snake venom toxins. *Neuron* 106:952-962.
2. Morales-Perez, C. L., C. M. Noviello, and R. E. Hibbs. 2016. X-ray structure of the human alpha 4 beta 2 nicotinic receptor. *Nature* 538:411-415.
3. Walsh, R. M., Jr., S. H. Roh, A. Gharpure, C. L. Morales-Perez, J. Teng, and R. E. Hibbs. 2018. Structural principles of distinct assemblies of the human alpha4beta2 nicotinic receptor. *Nature* 557:261-265.
4. Corringer, P. J., F. Poitevin, M. S. Prevost, L. Sauguet, M. Delarue, and J. P. Changeux. 2012. Structure and pharmacology of pentameric receptor channels: from bacteria to brain. *Structure* 20:941-956.

5. Cecchini, M., and J. P. Changeux. 2015. The nicotinic acetylcholine receptor and its prokaryotic homologues: structure, conformational transitions & allosteric modulation. *Neuropharmacology* 96:137-149.
6. Wang, G. K., and J. Schmidt. 1980. Primary structure and binding properties of iodinated derivatives of alpha-bungarotoxin. *J Biol Chem* 255:11156-11162.
7. Lester, H. A. 1972. Blockade of acetylcholine receptors by cobra toxin: electrophysiological studies. *Mol Pharmacol* 8:623-631.
8. Changeux, J., Z. Amoura, F. Rey, and M. Miyara. 2020. A nicotinic hypothesis for Covid-19 with preventive and therapeutic implications. *CR Biol* 343:33-39.
9. Bateman, A., M. Martin, C. O'Donovan, M. Magrane, E. Alpi, R. Antunes, B. Bely, M. Bingley, C. Bonilla, R. Britto, B. Bursteinas, H. Bye-A-Jee, A. Cowley, A. Da Silva, M. De Giorgi, T. Dogan, F. Fazzini, L. Castro, L. Figueira, P. Garmiri, G. Georghiou, D. Gonzalez, E. Hatton-Ellis, W. Li, W. Liu, R. Lopez, J. Luo, Y. Lussi, A. MacDougall, A. Nightingale, B. Palka, K. Pichler, D. Poggioli, S. Pundir, L. Pureza, G. Qi, S. Rosanoff, R. Saidi, T. Sawford, A. Shypitsyna, E. Speretta, E. Turner, N. Tyagi, V. Volynkin, T. Wardell, K. Warner, X. Watkins, R. Zaru, H. Zellner, I. Xenarios, L. Bougueleret, A. Bridge, S. Poux, N. Redaschi, L. Aimo, G. Argoud-Puy, A. Auchincloss, K. Axelsen, P. Bansal, D. Baratin, M. Blatter, B. Boeckmann, J. Bolleman, E. Boutet, L. Breuza, C. Casal-Casas, E. de Castro, E. Coudert, B. Cuche, M. Doche, D. Dornevil, S. Duvaud, A. Estreicher, L. Famiglietti, M. Feuermann, E. Gasteiger, S. Gehant, V. Gerritsen, A. Gos, N. Gruaz-Gumowski, U. Hinz, C. Hulo, F. Jungo, G. Keller, V. Lara, P. Lemercier, D. Lieberherr, T. Lombardot, X. Martin, P. Masson, A. Morgat, T. Neto, N. Nouspikel, S. Paesano, I. Pedruzzi, S. Pilbout, M. Pozzato, M. Pruess, C. Rivoire, B. Roechert, M. Schneider, C. Sigrist, K. Sonesson, S. Staehli, A. Stutz, S. Sundaram, M. Tognolli, L. Verbregue, A. Veuthey, C. Wu, C. Arighi, L. Arminski, C. Chen, Y. Chen, J. Garavelli, H. Huang, K. Laiho, P. McGarvey, D. Natale, K. Ross, C. Vinayaka, Q. Wang, Y. Wang, L. Yeh, J. Zhang, and U. Consortium. 2017. UniProt: the universal protein knowledgebase. *Nucleic Acids Res* 45:D158-D169.
10. McWilliam, H., W. Li, M. Uludag, S. Squizzato, Y. Park, N. Buso, A. Cowley, and R. Lopez. 2013. Analysis tool web services from the EMBL-EBI. *Nucleic Acids Res* 41:W597-W600.
11. Sievers, F., and D. Higgins. 2018. Clustal Omega for making accurate alignments of many protein sequences. *Protein Sci* 27:135-145.
12. Sali, A., L. Potterton, F. Yuan, H. Van Vlijmen, and M. Karplus. 1995. Evaluation of comparative protein modeling by modeler. *Proteins* 23:318-326.
13. Sali, A. 1995. Comparative protein modeling by satisfaction of spatial restraints. *Mol Med Today* 1:270-277.
14. Laskowski, R. A., M. W. Macarthur, D. S. Moss, and J. M. Thornton. 1993. Procheck - a program to check the stereochemical quality of protein structures. *J Appl Crystallogr* 26:283-291.
15. Campello, H. R., S. G. Del Villar, A. Honraedt, T. M. Viñas, A. S. F. Oliveira, K. E. Ranaghan, D. K. Shoemark, I. Bermudez, C. Gotti, R. B. Sessions, A. J. Mulholland, S. Wonnacott, and T. Gallagher. 2018. Unlocking nicotinic selectivity via direct C–H functionalisation of (–)-cytisine. *Chem* 4:1710-1725.
16. Oliveira, A. S. F., D. K. Shoemark, H. R. Campello, T. Gallagher, R. B. Sessions, and A. J. Mulholland. 2019. Identification of the initial steps in signal transduction in the α4β2 nicotinic receptor: insights from equilibrium and nonequilibrium simulations. *Structure* 27:1171-1183.
17. Søndergaard, C. R., M. H. Olsson, M. Rostkowski, and J. H. Jensen. 2011. Improved treatment of ligands and coupling effects in empirical calculation and rationalization of pKa values. *J Chem Theory Comput* 7:2284-2295.
18. Olsson, M. H., C. R. Søndergaard, M. Rostkowski, and J. H. Jensen. 2011. PROPKA3: consistent treatment of internal and surface residues in empirical pKa predictions. J *Chem Theory Comput* 7:525-537.
19. Jorgensen, W. L., J. Chandrasekhar, J. D. Madura, R. W. Impey, and M. L. Klein. 1983. Comparison of Simple Potential Functions for Simulating Liquid Water. *J Chem Phys* 79:926-935.

20. Lindorff-Larsen, K., S. Piana, K. Palmo, P. Maragakis, J. L. Klepeis, R. O. Dror, and D. E. Shaw. 2010. Improved side-chain torsion potentials for the Amber ff99SB protein force field. *Proteins* 78:1950-1958.
21. Bussi, G., D. Donadio, and M. Parrinello. 2007. Canonical sampling through velocity rescaling. *J Chem Phys* 126:014101.
22. Parrinello, M., and A. Rahman. 1981. Polymorphic transitions in single crystals: A new molecular dynamics method. *J Appl Phys*. 52:7182-7190.
23. Nosé, S., and M. L. Klein. 1983. Constant pressure molecular dynamics for molecular systems. Mo*l Phys* 50:1055-1076.
24. Essmann, U., L. Perera, and M. L. Berkowitz. 1995. A smooth particle mesh Ewald method. *J Chem Phys* 103:8577-8593.
25. Allen, M. P., and D. J. Tildesley. 1987. Computer simulation of liquids. Clarendon Press, Oxford, UK.
26. Abraham, M. J., T. Murtola, R. Schulz, S. Pall, J. C. Smith, B. Hess, and E. Lindahl. 2015. GROMACS: High performance molecular simulations through multi-level parallelism from laptops to supercomputers. *SoftwareX* 2:19-25.
27. Casalino, L., Z. Gaieb, J. A. Goldsmith, C. K. Hjorth, A. C. Dommer, A. M. Harbison, C. A. Fogarty, E. P. Barros, B. C. Taylor, J. S. McLellan, E. Fadda, and R. E. Amaro. 2020. Beyond shielding: the roles of glycans in the SARS-CoV-2 spike protein. *ACS Cent Sci* 6:1722-1734.
28. Delano, W. L. 2003. The Pymol molecular graphics system. version 0.98. Delano Scientific LLC, San Carlos, CA, USA.
29. DeLano, W. L. 2009. PyMOL molecular viewer: Updates and refinements. *Abstracts of Papers of the American Chemical Society* 238.
30. Oliveira, A., C. Edsall, C. Woods, P. Bates, G. Nunez, S. Wonnacott, I. Bermudez, G. Ciccotti, T. Gallagher, R. Sessions, and A. Mulholland. 2019. A general mechanism for signal propagation in the nicotinic acetylcholine receptor family. *J Am Chem Soc* 141:19953–19958.
31. Ng, H. W., C. A. Laughton, and S. W. Doughty. 2013. Molecular dynamics simulations of the adenosine A2a receptor: structural stability, sampling, and convergence. *J Chem Inf Model* 53:1168-1178.
32. Wang, C., D. Greene, L. Xiao, R. Qi, and R. Luo. 2017. Recent developments and applications of the MMPBSA method. *Front Mol Biosci* 4:87.
33. Genheden, S., and U. Ryde. 2015. The MM/PBSA and MM/GBSA methods to estimate ligand-binding affinities. *Expert Opin Drug Discov* 10:449-461.
34. Kumari, R., R. Kumar, A. Lynn, and O. S. D. D. Consortium. 2014. g_mmpbsa--a GROMACS tool for high-throughput MM-PBSA calculations. *J Chem Inf Model* 54:1951-1962.
35. Baker, N. A., D. Sept, S. Joseph, M. J. Holst, and J. A. McCammon. 2001. Electrostatics of nanosystems: application to microtubules and the ribosome. *Proc Natl Acad Sci U S A* 98:10037-10041.
36. Ibarra, A. A., G. J. Bartlett, Z. Hegedüs, S. Dutt, F. Hobor, K. A. Horner, K. Hetherington, K. Spence, A. Nelson, T. A. Edwards, D. N. Woolfson, R. B. Sessions, and A. J. Wilson. 2019. Predicting and experimentally validating hot-spot residues at protein-protein interfaces. *ACS Chem Biol* 14:2252-2263.
37. Wood, C. W., A. A. Ibarra, G. J. Bartlett, A. J. Wilson, D. N. Woolfson, and R. B. Sessions. 2020. BAlaS: fast, interactive and accessible computational alanine-scanning using BudeAlaScan. *Bioinformatics* 36:2917-2919.
38. Wood, C. W., J. W. Heal, A. R. Thomson, G. J. Bartlett, A. Ibarra, R. L. Brady, R. B. Sessions, and D. N. Woolfson. 2017. ISAMBARD: an open-source computational environment for biomolecular analysis, modelling and design. *Bioinformatics* 33:3043-3050.
39. McIntosh-Smith, S., J. Price, R. B. Sessions, and A. A. Ibarra. 2015. High performance in silico virtual drug screening on many-core processors. *Int J High Perform Comput Appl* 29:119-134.
40. Wrapp, D., N. Wang, K. S. Corbett, J. A. Goldsmith, C. L. Hsieh, O. Abiona, B. S. Graham, and J. S. McLellan. 2020. Cryo-EM structure of the 2019-nCoV spike in the prefusion conformation. *Science* 367:1260-1263.
41. Walls, A. C., Y. J. Park, M. A. Tortorici, A. Wall, A. T. McGuire, and D. Veesler. 2020. Structure, function, and antigenicity of the SARS-CoV-2 spike glycoprotein. *Cell* 181:281-292.

42. Daly, J. L., B. Simonetti, K. Klein, K. E. Chen, M. K. Williamson, C. Antón-Plágaro, D. K. Shoemark, L. Simón-Gracia, M. Bauer, R. Hollandi, U. F. Greber, P. Horvath, R. B. Sessions, A. Helenius, J. A. Hiscox, T. Teesalu, D. A. Matthews, A. D. Davidson, B. M. Collins, P. J. Cullen, and Y. Yamauchi. 2020. Neuropilin-1 is a host factor for SARS-CoV-2 infection. *Science* 370:861-865.
43. Lentz, T. L., T. G. Burrage, A. L. Smith, J. Crick, and G. H. Tignor. 1982. Is the acetylcholine receptor a rabies virus receptor? *Science* 215:182-184.
44. Hueffer, K., S. Khatri, S. Rideout, M. B. Harris, R. L. Papke, C. Stokes, and M. K. Schulte. 2017. Rabies virus modifies host behaviour through a snake-toxin like region of its glycoprotein that inhibits neurotransmitter receptors in the CNS. *Sci Rep* 7:12818.
45. Donnelly-Roberts, D. L., and T. L. Lentz. 1989. Synthetic peptides of neurotoxins and rabies virus glycoprotein behave as antagonists in a functional assay for the acetylcholine receptor. *Pept Res* 2:221-226.
46. Lan, J., J. Ge, J. Yu, S. Shan, H. Zhou, S. Fan, Q. Zhang, X. Shi, Q. Wang, L. Zhang, and X. Wang. 2020. Structure of the SARS-CoV-2 spike receptor-binding domain bound to the ACE2 receptor. *Nature* 581:215-220.
47. Yao, H., Y. Song, Y. Chen, N. Wu, J. Xu, C. Sun, J. Zhang, T. Weng, Z. Zhang, Z. Wu, L. Cheng, D. Shi, X. Lu, J. Lei, M. Crispin, Y. Shi, L. Li, and S. Li. 2020. Molecular architecture of the SARS-CoV-2 virus. *Cell* 183:730-738.
48. Ke, Z., J. Oton, K. Qu, M. Cortese, V. Zila, L. McKeane, T. Nakane, J. Zivanov, C. J. Neufeldt, B. Cerikan, J. M. Lu, J. Peukes, X. Xiong, H. G. Kräusslich, S. H. W. Scheres, R. Bartenschlager, and J. A. G. Briggs. 2020. Structures and distributions of SARS-CoV-2 spike proteins on intact virions. *Nature* 588:498-502.
49. Turoňová, B., M. Sikora, C. Schürmann, W. J. H. Hagen, S. Welsch, F. E. C. Blanc, S. von Bülow, M. Gecht, K. Bagola, C. Hörner, G. van Zandbergen, J. Landry, N. T. D. de Azevedo, S. Mosalaganti, A. Schwarz, R. Covino, M. D. Mühlebach, G. Hummer, J. Krijnse Locker, and M. Beck. 2020. In situ structural analysis of SARS-CoV-2 spike reveals flexibility mediated by three hinges. *Science* 370:203-208.
50. Casalino, L., A. Dommer, Z. Gaieb, E. P. Barros, T. Sztain, S. H. Ahn, A. Trifan, A. Brace, A. Bogetti, H. Ma, H. Lee, M. Turilli, S. Khalid, L. Chong, C. Simmerling, D. J. Hardy, J. D. C. Maia, J. C. Phillips, T. Kurth, A. Stern, L. Huang, J. McCalpin, M. Tatineni, T. Gibbs, J. E. Stone, S. Jha, A. Ramanathan, and R. E. Amaro. 2020. AI-driven multiscale simulations illuminate mechanisms of SARS-CoV-2 spike dynamics. bioRxiv, doi:10.1101/2020.11.19.390187 (preprint posted November 20, 2020).